THE PENNSYLVANIA STATE UNIVERSITY
SCHREYER HONORS COLLEGE

DEPARTMENT OF ENGINEERING SCIENCE AND MECHANICS

MULTI-SENSOR INVESTIGATIONS OF OPTICAL EMISSIONS AND THEIR RELATIONS TO DIRECTED-ENERGY DEPOSITION PROCESSES AND QUALITY

Christopher B. Stutzman
Spring 2018

A thesis
submitted in partial fulfillment
of the requirements
for a baccalaureate degree
in Engineering Science
with honors in Engineering Science

Reviewed and approved* by the following:

Abdalla R. Nassar
Assistant Research Professor at Applied Research Laboratory
Graduate Faculty of Engineering Science and Mechanics Department
Thesis Supervisor

Edward W. Reutzel
Associate Research Professor at Applied Research Laboratory
Graduate Faculty of Engineering Science and Mechanics Department
Co-thesis Supervisor

Akhlesh Lakhtakia
Charles Godfrey Binder Professor of Engineering Science and Mechanics
Honors Adviser

Judith A. Todd
Department Head
P.B. Breneman Chair and Professor of Engineering Science and Mechanics

*Signatures are on file in the Schreyer Honors College and the Engineering Science and Mechanics office.

Abstract

Additive manufacturing (AM) processes are limited in application by systematic and stochastic flaws that are produced during the process. In order to avoid this limitation, sensing strategies for the AM process are being developed. Using optical emissions spectroscopy and plume imaging, flaws generated during directed-energy deposition (DED) AM processes were investigated. Ti-6Al-4V coupons are built using varying laser power, powder flow rate, and hatching pattern to induce random and systematic flaws. Archimedes density measurements and X-ray computed tomography (CT) scans were completed on each part to determine flaw density and flaw locations. Three quantifiable metrics based on the state of the plume during processing were developed, analyzed and compared to the post-build CT scans: (1) line-to-continuum ratio around 430 nm, (2) line-to-continuum ratio around 520 nm, and (3) total plume area. For coupons built with constant laser power, variations in either powder flow rate or hatch pattern that led to an increase in flaw density were found to be accompanied by an increase in median line-to-continuum ratios around 430 and 520 nm and in total plume area. All three metrics appear to measure the same phenomena, i.e. they were internally consistent with each other. The conclusion is that optical emissions measured during DED processes can be used for flaw detection and presents a path forward for real-time flaw detection and assessment of build quality in DED and powder-bed-fusion processes.

Table of Contents

List of Figures iv

List of Tables v

Acknowledgments vi

1 Introduction 1

1.1 Motivations and The Impact of Additive Manufacturing . . . 2

1.2 Summary of Additive Manufacturing Processes . . . 4

1.3 Flaw Formation During DED Processes . . . 5

1.4 Process Monitoring Methods . . . 7

1.4.1 Melt-Pool Monitoring . . . 8

1.4.2 Optical-Emission Spectroscopy . . . 9

1.5 Outline of Thesis . . . 10

2 Methods 12

2.1 Materials And Processing Parameters . . . 13

2.1.1 Processing . . . 15

2.2 In-process Sensing . . . 16

2.2.1 Spectrometer . . . 16

2.2.2 Plume Camera . . . 17

2.3 Post-process Inspection . . . 18

2.3.1 CT scanning . . . 18
2.3.2 Archimedes Density . . . 19
2.4 Data Analysis . . . 20
2.4.1 Spectrometer – Line-to-Continuum Ratio . . . 20
2.4.2 Total Plume Area . . . 22
2.4.3 CT Scan Processing . . . 23
2.4.4 Graphical User Interface (GUI) . . . 24

3 Results and Discussion **26**
3.1 Isolated Flaws . . . 27
3.2 Median Plume Metrics and Total Flaw Density . . . 30
3.3 Internal Consistency . . . 33
3.4 Issues Encountered . . . 34
3.4.1 Inconsistencies in Archimedes Density . . . 35

4 Conclusions & Broader Impact **36**
4.1 Conclusions . . . 37
4.2 Future Work and Broader Impact . . . 38

A Block Diagrams for Matlab Codes **39**
A.1 Spectrometer Block Diagram . . . 40
A.2 Total Plume Area Block Diagram . . . 42
A.3 CT Image Processing Block Diagram . . . 44
A.4 GUI Block Diagram . . . 46

Bibliography **48**

List of Figures

2.1 Post-build image of one test coupon, scale is in cm. 13
2.2 (a) Parallel-hatching pattern. (b) Cross-hatching pattern. 15
2.3 Sensor layout within build chamber 16
2.4 Cubes mounted in the plastic tube to be CT scanned. 18
2.5 Archimedes density setup showing the balance, coupon holder, and the beaker of IPA used. 20
2.6 Intensity- and wavelength- calibrated spectra with known Ti I emission lines overlaid. 21
2.7 Parameters used in the line-to-continuum method. 22
2.8 Graphical user interface showing each metric plotted at a particular time step. . . . 25

3.1 (a) CT slice with a discontinuity in the ROI. (b) CT slice from the flaw-free ROI. . 28
3.2 (a) Plume image from the ROI with the discontinuity. (b) Spectral signal from the ROI with the discontinuity. 29
3.3 (a) Plume image from the flaw-free ROI. (b) Spectral signal from the flaw-free ROI. 29
3.4 Systematic flaws found in Run 008 (300 W, 4 g/min, parallel hatching). 30
3.5 (a) Median L2C 430 plotted against flaw density. (b) Median L2C 520 plotted against flaw density. (c) Median total plume Area plotted against flaw density. . . . 32
3.6 Linear relationship shown between two different metrics with a laser power of 475 W. 34

List of Tables

2.1 Summary of variables for each build 14
2.2 Summary of fixed parameters during all builds 14

3.1 Pearson correlation coefficient (r) between each metric pair 33

Acknowledgments

First, I thank my thesis advisors: Abdalla Nassar and Ted Reutzel for their continued support and assistance in the analysis of the data and the writing of this thesis. Without their assistance, this thesis would be nowhere close to the state it is in today. Second, I thank my parents Bruce and Susan Stutzman for their support in everything that I do. I would not be where I am today if they did not keep pushing me to do my best and to work toward my goals. Finally, I acknowledge Alex Dunbar for assistance with CT image analysis, Griffin Jones for assistance in the CT scanning of our coupons, Wesley Mitchell for assistance in running the deposition, Kevin Busko for assistance with the Archimedes density measurements, Ed Good for assistance in sample preparation, and my sister, Amanda Stutzman, for assistance in paper editing. This work was supported in part by the Office of Naval Research, under Contract No. N00014-11-1-0668. Any opinions, findings, and conclusions or recommendations expressed in this publication are those of the author and do not reflect the views of the Office of Naval Research.

Chapter 1

Introduction

1.1 Motivations and The Impact of Additive Manufacturing

Additive Manufacturing (AM) is revolutionizing manufacturing by enabling conventionally unattainable design freedom with little tooling and short lead-times. Recently, General Electric (GE) redesigned its jet engines to increase fuel efficiency and reduce emissions. Engineers at GE determined that an area of opportunity was to improve the fuel nozzle's design. The engineers then proceeded to design a more efficient nozzle, but they quickly found that the designs they created were much too complex for traditional manufacturing processes such as casting or brazing, because of the complex internal channels needed. Their solution was to additively manufacture the parts so that they could build the complex channels on a layer by layer basis instead of needing to go back and machine and assemble it later. Their result was the GE LEAP engine which reduced a system of 900 parts down to 16 [1]. But the application of AM is not just limited to industrial applications such as part consolidation and the development of parts containing complex geometries, it is an important tool in the medical industry as well. The ability to make a one-of-a-kind part to fit a specific patient has been a subject of interest for many years. A custom part makes it easier to match a person's body type and makes it more user friendly than a universal part. For example, the dental industry is using AM to produce dentures that exactly match a patient's anatomy and are a perfect replacement for their original teeth [2].

Additionally, AM has been analyzed for its environmental impact and the sustainability of the process. Chen et al. [3] discussed some of the environmental benefits that may be attainable using AM. They showed that scrap reduction was a positive aspect of the AM process because it reduced the amount of base material that had to be produced, shipped, and later recycled. In addition, they discussed the fact that an AM supply chain can be much shorter than a traditional supply chain because the parts can be produced on site or at a much closer facility. This reduces the transportation's contributions to the part's carbon footprint. They also discussed that AM leads to less overproduction, i.e., parts are only made when they are needed, thus reducing the number of parts in storage. This not only decreases the number of warehouses that must be built and maintained, but also reduces the amount of energy and material used to create the surplus parts. Finally, they discussed some of the potential negative environmental impacts, such as the large amount of energy used in the process to form the feedstock and deposit the part. Huang et al. [4], determined that the high energy consumption used in the production of AM parts is actually lower than that of a conventionally formed part. They looked at different aspects of the process and determined that a significant energy savings is found when only producing parts that are needed, i.e., not producing a warehouse of replacement parts. In addition, they determined that AM parts are typically lighter than a conventionally formed part. This leads to an energy savings in the aerospace industry.

Finally, AM has use for the repair of parts. Traditionally, when a part is worn out, it is replaced with a brand new identical part. One issue is that this requires a large warehouse full of replacement parts which are often located away from the object's location, requiring time to find and ship the part. AM provides the ability to deposit new material atop a worn part, permitting reuse of the part. This reduces the typical lead-time for a replacement part, and allows the repair of parts in remote locations. Frazier et al. [5] discussed the repair of turbine blades in the Army using a laser engineered net shaping (LENS) system. Additionally, Mudge et al. [6] discussed the repair of driveshafts and the cladding of oil-field components using the LENS process.

While AM has seen significant growth in many areas, qualification of the process, especially for critical applications, remains a significant hurdle. In-situ process monitoring and detection of flaws and defects – defined as discontinuities "that by nature or accumulated effect render a part or product unable to meet minimum applicable acceptance standards or specifications" [7] – offers a promising opportunity to assist in the qualification process. By detecting flaws during processing, a build can either be aborted to curtail losses or repaired to produce a flaw-free part.

1.2 Summary of Additive Manufacturing Processes

Additive Manufacturing describes a wide range of manufacturing processes where a component is built layer by layer. This is in contrast to traditional, subtractive manufacturing processes, where material is removed from a component to add a feature to the part (e.g. machining or cutting). Within AM, there are many possible feedstocks, including polymers, metals, and bio-materials, and different manufacturing processes (e.g. powder bed fusion (PBF), directed energy deposition (DED)) [8]. Here, the focus is on laser-based, powder-fed, directed-energy deposition (DED).

Laser-based DED is a process in which a laser provides energy to the substrate, forming a small melt-pool. As the melt-pool is being formed, feedstock is introduced into the melt-pool. In powder-fed DED, powder is blown into the melt-pool using an inert assist gas, such as argon. A portion of the powder ($< 100\%$) is captured by the melt-pool and increases the melt-pool volume. Tracks (single lines of deposited material) are formed by translating the substrate relative to the laser and powder flow. Layers are formed by depositing overlapping tracks adjacently until the desired 2-D shape is attained. Parts are then formed by depositing layers atop prior layers until the desired 3-D geometry is achieved. This processing typically occurs within an inert environment to avoid contamination and oxide formation during deposition [9].

Within a DED process, there are numerous processing parameters that can be changed. Corbin et al. [10] determined the effect of common processing parameters including laser power, travel speed, working distance, substrate preheat, and track order on the deposition of Inconel 718. They found that increasing the travel speed decreased the height of the track, whereas increasing working distance increased the height, and increasing laser power increased the height but to a lesser extent. Furthermore, they determined that increasing laser power leads to an increase in track width, and a decrease in travel speed leads to a decrease in track width. Working distance was shown to have little effect on the width of the track. They additionally showed that substrate preheat can increase the track width and height by 10.5% and 22.2%, respectively. Finally, it was shown that track order had very little effect on both track height and width. Wang et al. also studied the effects of laser power on the deposition process of 304L stainless steel [11]. They found that walls built with higher laser power had larger grain sizes than walls built with lower laser power. They concluded that higher laser power yields a larger melt-pool. This melt-pool then has a smaller thermal gradient than a smaller melt-pool, thus cooling more slowly. A slow cooling rate leads to increased grain growth. Through this grain growth, the mechanical properties are degraded, as explained by the Hall-Petch relationship which relates grain size to yield strength [11]. Generally, if the component contains small grains, it will have a higher yield strength than a component with large grains. In summary, there are many parameters that can be controlled within a DED process, each with its own effect on the dynamics of the process and the condition of the resulting part. As such, it is important that proper processing parameters are selected to produce high-quality components.

1.3 Flaw Formation During DED Processes

Flaws are often generated during DED processes and can be classified into two major categories, inter- and intra- layer flaws. Inter-layer flaws occur between two deposited layers, while intra-layer flaws are formed within a layer. Flaws are often further classified into two categories: porosity, and lack-of-fusion. Lack-of-fusion is caused when insufficient energy is provided to fully melt a current track and partially melt neighboring and underlying tracks. These flaws are often caused by improper processing parameter selection, and are mitigated by optimizing the laser power and powder flow rate. Keyhole pores can be formed when using a high-power energy source. If sufficient energy is provided to the melt-pool, the laser-material interaction can transfer from conduction mode to keyhole mode. Instabilities in the keyhole can cause it to collapse and form a pore. Finally, gas porosity is formed by a combination of porosity within the powder, and absorption of the inert process gas. See DebRoy et al. [12] for further discussion regarding mechanisms of flaw formation in DED.

According to Susan et al. [13], inter-layer lack-of-fusion flaws, are typically elongated with an irregular shape. In contrast, intra-layer porosity, or gas porosity, is typically spherical in shape and does not correspond to a physical feature of the part (i.e. layer, microstructure, etc.). In addition, lack-of-fusion flaws are typically more prevalent near the substrate. It is postulated that this effect is due to heat dissipation by the substrate [13]. On successive layers, the temperature of the coupon increases, and the deposition surface is effectively preheated, thus reducing the energy needed to form the deposition. Ashan et al. [14] investigated the effect of powder-atomization technology and processing parameters on the deposition of Ti-6Al-4V. They discovered that powder feedstock formed using gas atomization has a higher volume of pores in the powder than a plasma rotating electrode (PREP) powder. It was shown that coupons built with PREP powder have a lower level of intra-layer porosity as compared to the gas-atomized powder, for the same processing parameters. Additionally, they determined that an increase in powder flow rate decreased the coupon porosity up to a certain value (0.066 g/s), beyond which the porosity value began to increase again. Finally, they determined that coupons built with PREP powder have, on average, larger pores than gas-atomized powder. Wang et al. [15] found that AISI 316L coupons built with a higher oxygen content in the build chamber tended to have larger inter-layer porosity values. The pores were irregularly shaped and appeared to be the coalescence of many pores. They postulated that this effect was caused by oxidation, and that oxides likely remain in the solid state during melting and affect the wetting of the material. Inter-layer porosity was accompanied by un-melted powder particles.

Systematic flaws such as lack-of-fusion and porosity are formed while processing with constant, unoptimized input parameters. The selection of optimized input parameters, leading to a reduction in systematic flaws, has been the topic of many research efforts. However, it has been observed that random or stochastic flaws also occur during processing with optimal parameters, i.e. these flaws are not systematic. Unfortunately, there have been few studies on stochastic flaws, and the processes that underlie their formation are poorly understood. Therefore, the need for process monitoring is two-fold. First, input parameters such as laser power, powder flow rate, etc. need to be monitored to ensure that the input parameters are appropriate to prevent the formation of systematic flaws, and also to validate that no processing parameter shifts occur during processing.

The second need for process monitoring involves the detection of anomalies and stochastic flaws that may occur during processing. If such flaws are identified in real time, it is likely possible to remelt and repair the flaw before the deposition of subsequent layers. Since stochastic flaw formation and prevention is poorly understood, the detection of these flaws is important to ensure that quality parts are manufactured.

1.4 Process Monitoring Methods

Process monitoring is receiving a lot of attention for the DED process as a means to ensure that internal flaws are detected and that all specifications are met. While many post-process analysis methods exist for metallic materials, these processes are expensive and requires a part to be fully developed before inspection. In-situ sensing determines the quality of the part before all subsequent value-added processes are performed on the part, thus curtailing material and time losses that would be incurred by completing the deposition and producing a failed part. Different approaches have been investigated toward in-situ sensing and control of AM builds, as outlined in survey and review articles [16, 17, 18, 19, 20, 21, 22].

Sensors that have been applied to DED include acoustic sensors, image-based sensors, spectrometers, and temperature sensors. Acoustic monitoring is mainly used to investigate phase transformations, crack formation, weld surface flaws, and plasma fluctuations. Electromagnetic acoustic transducers (EMATS) can be used to detect voids in a weld but are not well developed for use in AM processes yet. Coaxial cameras can be used to determine the size and shape of the melt-pool, while a coaxial photodiode can measure the temperature of the melt-pool. Additionally, two-color pyrometers have been used to measure the average melt-pool temperature. Spectrometers have been proven useful to analyze the composition of the plasma plume, and suggests that a correlation between optical emissions and flaws in the part may be present. Another approach is to use thermocouples to measure the melt-pool temperature directly. Sensor data can also be fed into controllers to adjust processing parameters. Temperature measurements have been successfully fed into a controller to adjust incident laser power by either increasing wattage, or changing the stand off distance. Many sensing and control methods fall into two major categories: melt-pool monitoring and optical emission spectroscopy.

1.4.1 Melt-Pool Monitoring

By far, melt-pool sensing using infrared cameras, pyrometers, and thermocouples is among the most popular techniques within the research community [23, 24, 25, 26, 27]. Hu et al. [23] demonstrated the use of a CCD camera filtered to near-infrared wavelengths (NIR) to monitor the temperature of the melt-pool. This technique requires the emissivity of the melt-pool to be known. Here they chose a static emissivity value of 0.3 and used this value consistently throughout the experiment. The temperature of the melt-pool can then be calculated using a modified version of Wien's Law. They were able to then use this information for closed loop control and simulation of the process. Kriczky et al. [24] demonstrated the use of a coaxial two color pyrometer to measure thermal metrics of the melt-pool. By examining the ratio of two different emission line in the NIR - IR range, a temperature measurement of the melt-pool can be acquired. They used this technique to develop a series of thermal metrics such as the length-to-width ratio, and the maximum melt-pool temperature. Craeghs et al. [25] showed that a filtered photodiode could serve as a proxy for the melt-pool size, and a filtered high-speed CMOS camera could be used as a proxy for melt-pool temperature. This information was then used as feedback to control the process. Furumoto et al. [26] also utilized a two color pyrometer to measure the melt-pool temperature. They used two different targets each with a thermocouple to calibrate the pyrometer. They also used a cut-off filter to remove the effect of the laser beam. This cut-off filter effectively removed all radiation below 1600 nm. In addition, they used a high speed camera with a metal halide illumination lamp to measure the consolidation of powder particles as the process continued. Finally, Hu et al. [27] also used an infrared camera to monitor the temperature and size of the melt-pool. Here, a filter was included in the setup to reduce the influence of high-intensity light from the process. In addition, they used a separate camera filtered to a certain wavelength to verify the size of the melt-pool that was measured with the infrared camera. They were able to use this information to determine the gray level isotherms which are directly related to thermal gradients in the part. They used this information to create a more accurate finite element model of the process.

While each of these articles provides a useful approach to monitoring the process, these techniques are often limited in practice. IR cameras require the emissivity of the melt-pool to be known and often assume that this emissivity is constant through the entire process. Additionally, the measurements from these sensor are often limited by interactions with the highly excited plasma that is formed above the laser-interaction zone. To allay these concerns, alternative sensing strategies for AM involves monitoring and analyzing spectral emissions from the vapor/plasma plume generated during the laser-material interaction.

1.4.2 Optical-Emission Spectroscopy

Optical-emission spectroscopy (OES) has been used for many years in sensing laser processes. Early work applied conventional OES techniques to plumes generated during CO_2-laser welding of stainless steel and titanium, and showed that the metal-vapor plume is likely in a state of local thermodynamic equilibrium (LTE) [28]. This conclusion was used to justify the use of spectral linewidth measurements for electron density and temperature calculations, and the use of relative line emissions for estimation of electron temperatures within the plume [29, 30]. Using the ratio of emission lines, i.e., the Boltzmann plot technique, Ancona et al. [31] measured the excitation temperatures of iron, chromium, and magnesium vapors during CO_2-laser welding of AISI 304 stainless steel and found that welding quality correlates with temperature fluctuations in one or more species. OES has also been used in CO_2-laser welding to study the effects of gas shielding [32], vaporization [28, 33], and weld quality [34]. Processing regimes have been optimized and oxidation has also been assessed during CO_2-laser nitriding of titanium via OES-based plume imaging [35]. Tewari et al. [36] also showed that, for CO_2-laser cladding of a niobium-based alloy, clad thickness, and the concentration of alloying elements are related to the intensities and ratios of Nb, Hf, and Al emission lines. Using a system of six (6) optical sensors, including photodiodes, spectrometers, and cameras, You et al. [37] demonstrated that optical emissions can be used to develop and validate a non-linear model of the laser welding process.

More recently, OES has been applied to sense DED AM processes. Song and Mazumder [38] demonstrated the ability to measure chromium content during the deposition of pure chromium onto H13 Tool Steel. In subsequent work, they showed that spectral line-emission ratios were indicative of phase transformations [39]. In addition, Ya et al. [40] showed that iron-line intensity ratios are indicative of process stability in laser deposition processes, and the electron temperature can be indicative of clad dilution. Bartkowiak [41] demonstrated that spectral emissions vary greatly with laser power or scan speed. Song et al. [42] further demonstrated that support-vector regression can be used to increase the accuracy of in-situ composition measurements. Contrary to other in-situ composition measurements that are affected by the intensity of the laser, they were able to achieve an accurate composition prediction across a range of laser power. Liu et al. [43] demonstrated that spectral emissions were indicative of clad instabilities in the laser cladding process. Nassar et al. [44] recently demonstrated that line-to-continuum ratios about certain spectral lines may be used to detect lack-of-fusion flaws generated during the laser directed energy deposition (DED) process. Recently, work by Nassar et al. [45] illustrated that plume geometry is closely related to processing parameter variations for laser deposition processes.

1.5 Outline of Thesis

This work investigates the use of OES and plume imaging for monitoring of DED processes. Section 2.1 summarizes the key DED AM processing parameters — including laser power, powder flow rate, and hatch pattern — that were varied to induce flaws in the coupons. Section 2.2 presents the procedures used to capture and analyze the optical emissions that were generated during the process. A summary of each sensor, its purpose, and the data that was captured is also summarized in this section. Additionally, the Matlab scripts that were written to process and analyze the data are summarized in Appendix A to fully describe the tools that were developed to analyze the data.

Section 2.3 details the procedures that were followed to analyze the data, and the equations used to calculate the line-to-continuum ratio, as well as the total plume area and flaw density.

Chapter 3 presents the results and analysis of the experiments, namely that metrics calculated from optical emissions do indeed correlate to flaws detected in a coupon. Section 3.1 demonstrates that isolated flaws in an otherwise flaw-free coupon can be detected through large increases in total plume area, as well as the intensity of spectral emissions. Section 3.2 shows that median plume metrics — line-to-continuum ratios around 430 and 520 nm, and total plume area — can be correlated to the total flaw density of a coupon. In other words, as the median of each plume metric increases in value (for a constant laser power), a corresponding increase in flaw density is observed. Section 3.3 presents the concept of internal consistency. Here it is verified that each plume metric is indeed measuring the same phenomena, i.e., the excitation of the plasma plume. By calculating the Pearson correlation coefficient, each combination of plume metrics is shown to have a linear relationship and therefore is internally consistent.

Portions of this thesis have been previously published by Stutzman et al. [46]. The author's contributions to that work included conducting experiments, analyzing and reporting experimental results, as well as formulating hypotheses based on observations. Such material is reprinted here with the permission of the author and the journal of additive manufacturing.

Chapter 2

Methods

The material in this section describes the materials, processing parameters, sensors and data processing methods used in this experiment. Section 2.1 describes the materials and parameters used in the experiment. Section 2.2 describes the sensing setup that was implemented, including a short description of each sensor. Section 2.3 concludes this chapter with a description of the post-processing inspection methods used.

2.1 Materials And Processing Parameters

Design of the test experiments involved many considerations to account for differing processing conditions and to allow for position synchronization during the data analysis process. The coupons were built using Ti-6Al-4V feedstock manufactured by EOS (spherical, argon-atomized powder with a D50 of 37.72 microns). A rectangular test coupon, as shown in Figure 2.1, was chosen with dimensions of 15 x 15 x 10 mm (l x w x h) which yielded 12 hatches per layer and a total of 40 build layers. The coupon was deposited upon a 6.35 mm (0.25 inch) thick rolled Ti-6Al-4V substrate. In addition, a small 90^o deposition was deposited on a known corner of the substrate to allow for position registration during data analysis.

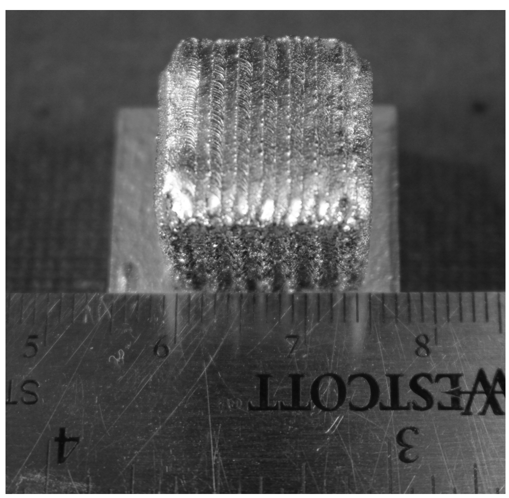

Figure 2.1: Post-build image of one test coupon, scale is in cm.

A set of processing conditions, summarized in Table 2.1, were chosen to replicate processing condition shifts that could occur during a DED process, e.g. laser power may decrease due to increasingly dirty optics, and would likely result in systematic and random flaws being generated. Each coupon was built with one combination of processing conditions and these processing conditions remained constant throughout the entire deposition. In addition, the parameters listed in Table 2.2 were held constant through all coupons builds. Processing took place in an argon environment, and chamber conditions were regulated to a gauge pressure of 1-3 inches of water (0.25–0.75 kPa) with a starting oxygen concentration of less than 20 ppm.

Table 2.1: Summary of variables for each build

Run #	Laser Power (W)	Powder Flow Rate (g/min)	Hatch Pattern
1	300	2	Parallel
5	300	2	Cross
6	300	3	Parallel
7	300	3	Cross
8	300	4	Parallel
9	300	4	Cross
11	425	2	Cross
12	425	3	Parallel
13	425	3	Cross
20	475	4	Parallel
22	475	4	Cross

Table 2.2: Summary of fixed parameters during all builds

Constants	
Speed (mm/s)	10.6
Layer Spacing (mm)	0.254
Hatch Spacing (mm)	1
Hatches per layer	12
Layers per sample	40

Two different hatching strategies, as shown in Figure 2.2, were used to build the coupons. The parallel-hatching pattern used build vectors that were parallel to each other on adjacent layers. In contrast, the cross-hatching pattern rotated all build vectors 90^o between each layer. For both cases the direction of each hatch reversed between hatches.

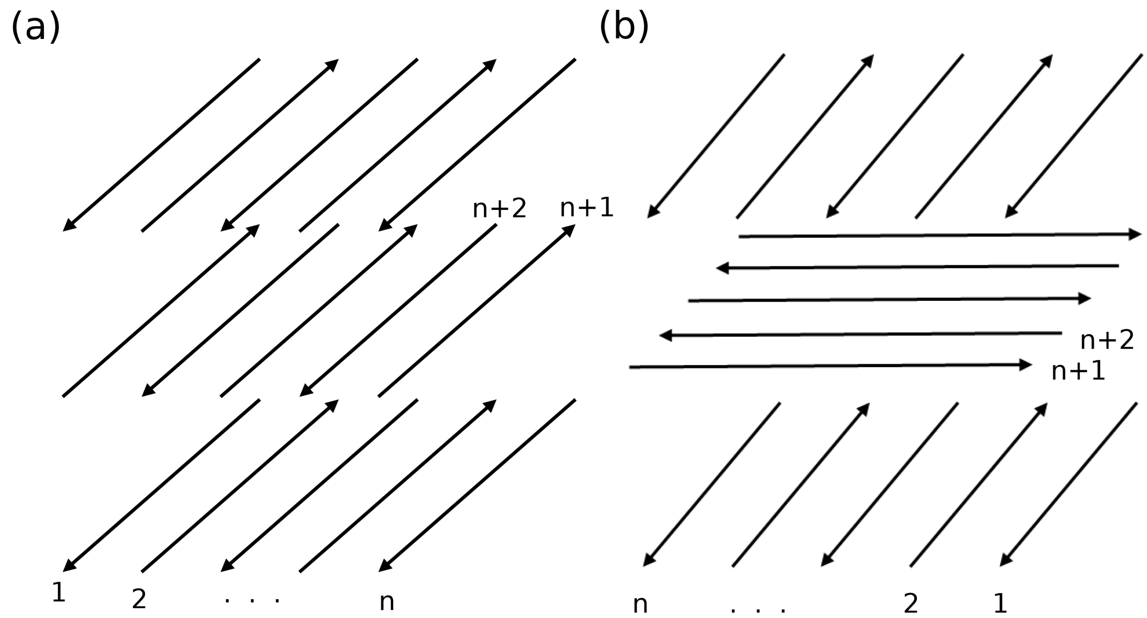

Figure 2.2: (a) Parallel-hatching pattern, (b) Cross-hatching pattern

2.1.1 Processing

The coupons were built in an Optomec LENS MR-7 DED system. The LENS system is a DED system with a work area of 300 x 300 x 300 mm within a controlled-atmosphere chamber. This chamber is filled with an inert shielding gas such as argon, and contains a gas purification system that removes O_2 from the chamber and recirculates the gas to ensure that the oxygen content remains below a set ppm value. The LENS machine uses three different axes: x,y,z to build each coupon. Coupons are moved linearly along the x-y directions on a pair of stages, while the laser is moved in the z direction using a third linear stage. This system uses a 500 W (maximum) IPG Ytterbium-doped fiber laser for deposition. The second-moment diameter of the beam at the substrate was 1.24 mm, as measured with a Primes GmbH FocusMonitor system. Powder is provided to the melt-pool using two independent powder feeders, each capable of holding ~2 L of powder [47].

A stock LENS machine uses OEM control software and machine-code to control the build process. The system that was used in this experiment has been modified to use custom control software to control the powder flow, stage position, laser stand off distance, and laser status. This custom software allows more direct control of process parameters than would be available in the stock LENS software. This software also enables direct connection of custom data acquisition equipment to ensure accurate position and time data synchronization.

2.2 In-process Sensing

Position and time synchronized data were collected during the deposition of all coupons using three different sensors. The sensors included a UV-VIS-IR spectrometer, four filtered photodiodes, and a camera filtered to 430 nm. The sensors were mounted in the Optomec LENS MR-7 system as shown in Figure 2.3 and were focused such that they observed the laser-material interaction zone. Additional sensor details are provided in Sections 2.2.1 and 2.2.2.

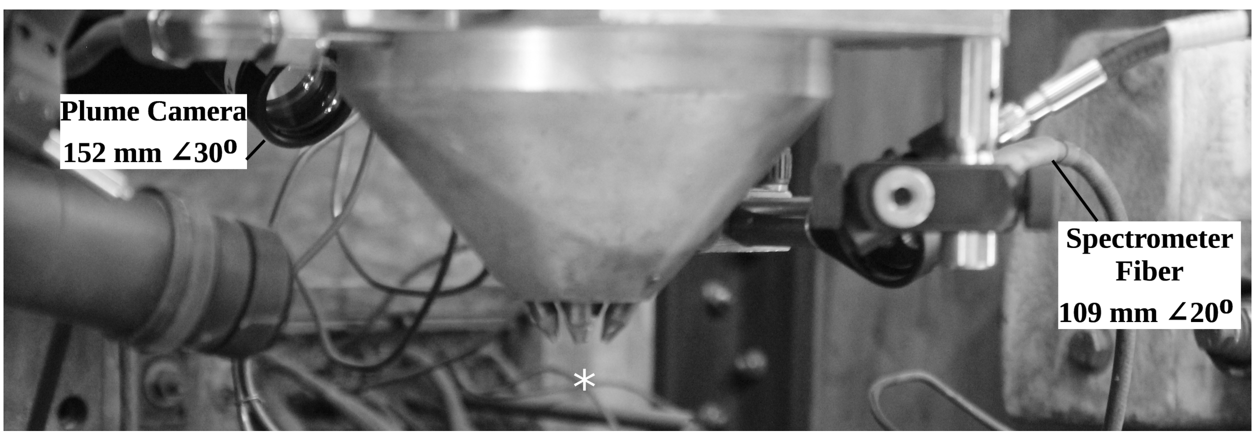

Figure 2.3: Sensor layout within the build chamber. ”*” represent the approximate location of the laser-material interaction zone.

2.2.1 Spectrometer

An Ocean Optics HR2000+ UV-VIS-IR spectrometer was used to collect uncalibrated spectra from the light emitted by the laser-interaction zone during the deposition of each coupon. The spectrometer was configured to integrate the light received for 20 ms and then save that spectrum, along with its corresponding position and time, to a comma-seperated-variable (CSV) file. A single-core fiber optic patch cable (600 μm, 0.22 NA) was used to connect the HR2000+ spectrometer to a fiber optic mount within the build chamber. A cover glass was used to protect the end of the bare fiber during deposition.

2.2.2 Plume Camera

Plume images were captured using a Basler Pilot piA640-210gm CCD camera with a resolution of 648 by 488. This camera was coupled to a 430 nm band-pass filter to image Ti I emissions that were present in the plume. The choice of 430 nm will be discussed further in Section 2.4.1. The plume camera was configured with an exposure time of 10 ms with a new frame being returned every 20 ms. These frames were then saved with names corresponding to the image's position and time. The plume camera was mounted in the rear of the build chamber and was focused to image the region directly above the laser-material interaction zone. A series of calibration tests were performed in which a grid of known area was placed on a build plate at the laser-material interaction zone. This grid was then imaged by the plume camera producing an image from the perspective of the camera. This image was then imported into an image processing program and the number of pixels in several parts of the grid were calculated. Using the known grid dimension, a pixel per millimeter value of 55 $\frac{pixels}{mm}$ was calculated and used to calculate the total plume area as detailed in Section 2.4.2. Further calibration, including image transformation, was attempted on the calibration grid image, but upon calculation of the error between the transformed image and the as-captured image, it was determined that using the as-captured image would sufficiently represent the plume's condition for this work. In addition, it was determined that applying a geometric transformation was impractical with the volume of data that was produced and would lead to significantly higher computational time than using as-captured images.

2.3 Post-process Inspection

Post-build non-destructive evaluation of flaws (NDE) methods were used to determine the quality of parts produced. X-Ray computed tomography (CT) and Archimedes density were each used to determine a different quality aspect of the part.

2.3.1 CT scanning

CT scans were performed on the coupons using a GE phoenix v|tome|x m 300 system. A 300 kV source was used to scan each of the parts. The coupons were packed in a square tube, one above the other, as shown in Figure 2.4 and the entire tube was scanned all at once. The scans were performed with a reconstructed voxel resolution of $\sim$ 15 microns per voxel.

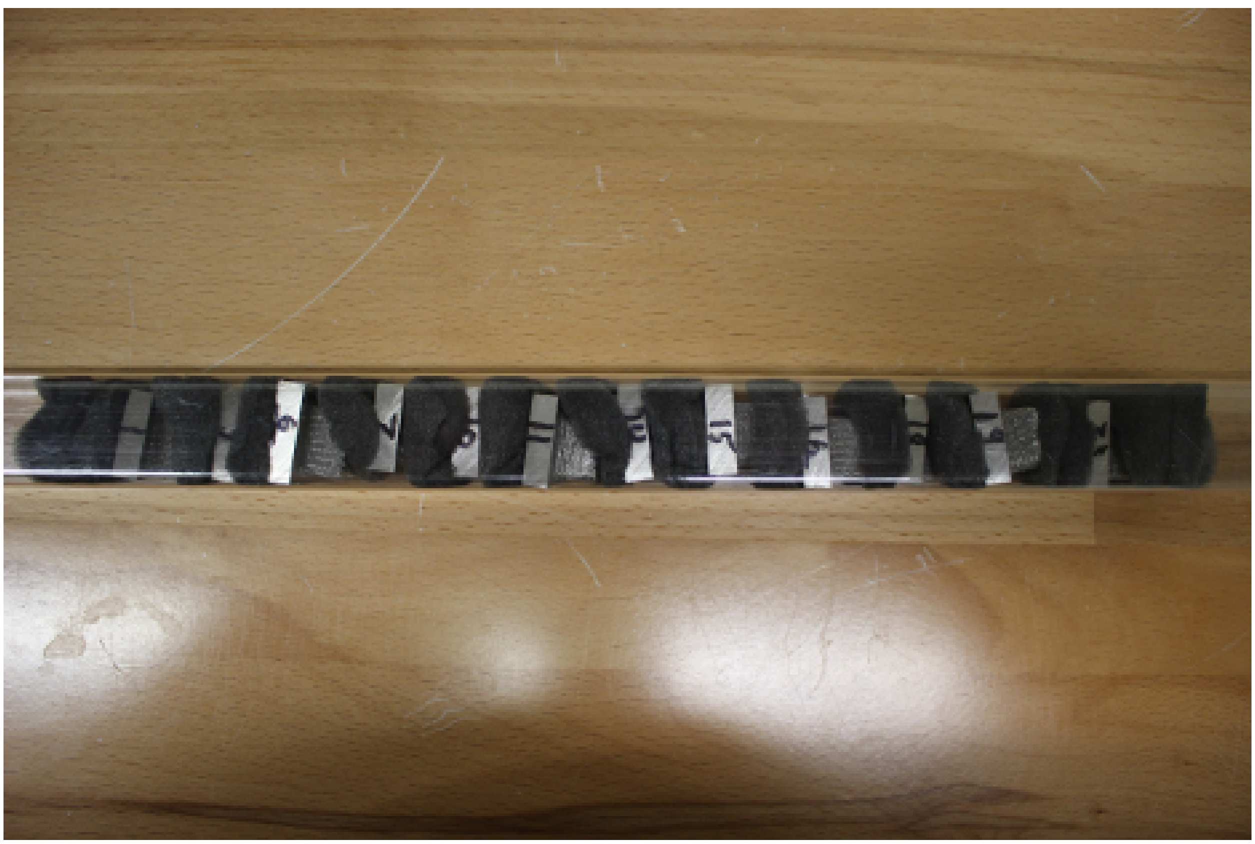

Figure 2.4: Cubes mounted in the plastic tube to be CT scanned.

2.3.2 Archimedes Density

To assess the volume of internal porosity, Archimedes density measurements were performed on the coupons using a Scientech SA-525D mass balance, as shown in Figure 2.5. This balance has a resolution of 1 mg with a standard deviation of 0.5 mg. First, a coupon was placed on the balance, and the dry weight of the coupon was recorded. Next, the coupon was suspended on a wire holder within a beaker of 99 %, technical-grade isopropyl alcohol (IPA). Once suspended within the IPA, the part was visually inspected to ensure that no air bubbles formed on the surface of the coupon. Once the surface was guaranteed to be bubble-free, the weight of the suspended coupon was recorded. This process was then repeated for each coupon, and each coupon was repeated a total of three times. The Archimedes density was calculated as

$$\rho_{coupon} = \rho_{ipa} \frac{W_a}{W_a - W_{IPA}} \quad , \tag{2.1}$$

where ρ_{coupon} is the density of the coupon, ρ_{ipa} is the density of the IPA, W_a is the weight of the coupon in air, and W_{IPA} is the weight of the coupon in IPA.

IPA, rather than water, was chosen due to the very high surface roughness of the coupons. IPA has a much lower surface tension (roughly a third less than water) and is therefore able to wet the rough surface much more completely than water. The scale was last calibrated in July of 2014, which may induce some errors in the measurements. The scale was zeroed between each measurement to ensure consistency between measurements.

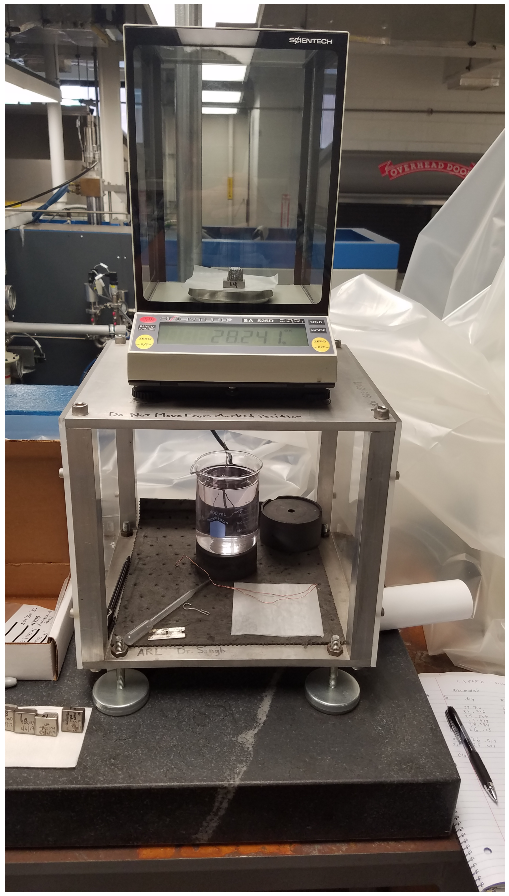

Figure 2.5: Archimedes density setup showing the balance, coupon holder, and the beaker of IPA used.

2.4 Data Analysis

The line-to-continuum ratios around 430 and 520 nm and the plume area measurements were automatically indexed to the stage position, and the system's clock during data acquisition. Data collected during NDE testing were processed to calculate coupon flaw density.

2.4.1 Spectrometer – Line-to-Continuum Ratio

Each spectrometer intensity reading was saved in a CSV file with its corresponding position and time information. This CSV file was then processed using a custom Matlab script, whose block diagram is shown in Appendix A.1.

A line-to-continuum ratio, described by Nassar et al. [44], about two separate spectral lines was used in this experiment to describe the excitation of the plume. The two spectral lines used in this experiment were specifically chosen because they coincided with strong, atomically-excited Titanium (Ti I) emission lines, as based on data from NIST [48]. Excited Ti species are expected within the plasma due to the extremely high melt temperature and the vaporization that is observed during the build process. In particular, we chose to look at Ti I emission lines at 430 and 520 nm because they had an adjacent spectral region which was free from line emissions, as shown in Figure 2.6.

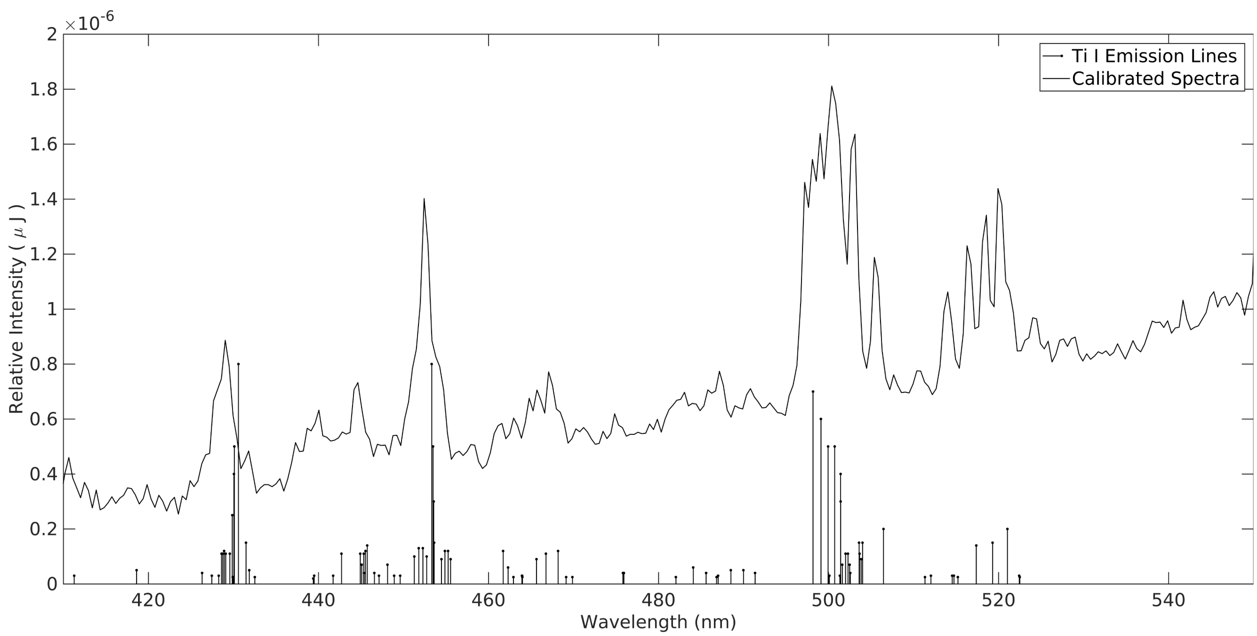

Figure 2.6: Intensity- and wavelength- calibrated spectra with known Ti I emission lines overlaid.

Choosing an adjacent region free from line emissions was required to calculate the continuum emission during the process. The line-to-continuum ratio was calculated, around a given spectral line, as follows.

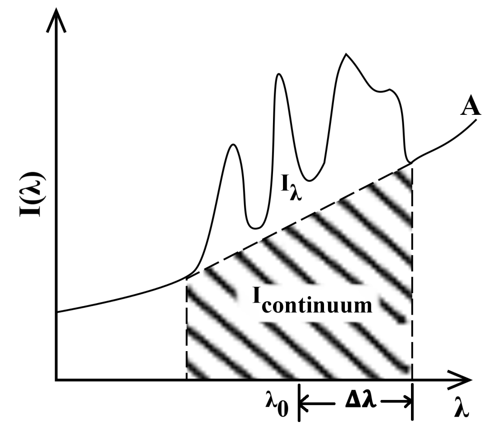

Figure 2.7: Parameters used in the line-to-continuum ratio method.

$$I_{Continuum} = \int_{\lambda_0-\Delta\lambda}^{\lambda_0+\Delta\lambda} \frac{I(\lambda_0+\Delta\lambda) - I(\lambda_0-\Delta\lambda)}{2\Delta\lambda} \cdot \lambda d\lambda + I(\lambda_0-\Delta\lambda) d\lambda \tag{2.2}$$

Equation 2.2 is used to integrate below curve A, shown in Figure 2.7, to determine the continuum emission, $I_{continuum}$, within a wavelength window of width $2\Delta\lambda$. Within the wavelength window, $2\Delta\lambda$, curve A is approximated by a line. The wavelength window is centered around λ_o, which is the central wavelength.

The line emission intensity within the wavelength window, $2\Delta\lambda$, is calculated by

$$I_{\lambda_o} = \int_{\lambda_0-\Delta\lambda}^{\lambda_0+\Delta\lambda} I(\lambda) d\lambda - I_{Continuum} \quad , \tag{2.3}$$

which integrates the area between the spectral emissions, $I(\lambda)$, and curve A, as shown in Figure 2.7. The line-to-continuum ratio was then calculated as $\frac{I_{\lambda_o}}{I_{continuum}}$.

2.4.2 Total Plume Area

Each plume image was saved with its position and time stamp embedded in the name of the file. These images were then processed using a custom algorithm in an object-oriented Matlab function, whose block diagram is shown in Appendix A.2.

The total plume area was calculated to describe the size of the plasma plume formed above the laser-material interaction zone during the process. First, a threshold was applied to each grayscale plume image, converting the grayscale image into a binary image with white pixels being ones and black pixels being zeros. The threshold here was set manually by varying the global threshold value until the entire plume was seen distinctly in the resulting binary image. This same threshold was then used for every plume image processed, thereby ensuring consistency between images. Next the sum of all pixels within the image was found by summing along each column in the image matrix. Next, the sum of the light pixels was multiplied by the square of the conversion factor that was determined in Section 2.2.2, to yield an estimate of the total plume area in square millimeters.

2.4.3 CT Scan Processing

Each coupon was CT scanned to calculate its flaw density, and to determine the morphology and location of flaws. In order to compare the position- and time- synchronized data to the post-build CT scans, each CT dataset was manually rotated and translated to (approximately) register the CT volume to the same coordinate system used for all sensor data captures. Next, a series of TIFF image stacks (corresponding to the 15 μm voxel size) were created along planes normal to the build-up direction, i.e. along the z axis, using VGSTUDIO MAX (VOLUME GRAPHICS CORPORATION).

Next, a custom Matlab script was used to calculate the flaw density of the part. The algorithm is summarized in a block diagram in Appendix A.3. A manual threshold was then applied to each slice in the image stack to convert the grayscale images into binary images where dense material had a pixel value of one and flaw/void material had a pixel value of zero. The manual threshold was chosen to ensure consistency between image slices, and was chosen such that the voids were distinct from the surrounding dense material. This threshold remained unchanged for every coupon scanned. Next, a background subtraction (i.e. illumination correction) was applied to all images to correct for x-ray artifacts. To eliminate complications arising from edge effects, analysis of the CT data was limited to the interior of each part, approximately 1.9 mm away from the edges. Voids with fewer than 4 connected pixels were eliminated from further analysis. The porosity level within the part (flaw density) is defined as the ratio of void pixels to all pixels within the interior of the coupon, and corresponds to the volume ratio of flaws to dense material. Here, we explicitly define average flaw density calculated on a layer by layer basis as

$$D_{flaw} = \frac{\sum_{n=1}^{n=layers} \frac{P_d - P_l}{P_d}}{layers} \quad , \tag{2.4}$$

where D_{flaw} is the density of flaws within a stack of binary CT images. Each CT image constitutes a CT-layer, n, with a layer spacing equal to the voxel size. P_d is the number of fully-dense pixels (flattened voxels) within the region of interest(ROI) on an ideal CT-layer and P_l provides the total number of dense (white) pixels within the ROI on layer n. If P_d is constant for all layers, as in this experiment, then the average flaw density is equivalent to the true flaw density of the part. After processing, the line-to-continuum ratios around 430 and 520 nm and the plume area were compared against the location of lack-of-fusion flaw and related to flaw density within built components. A limitation of this alignment method is the variability in deposition thickness at each layer, since over- or under-building are common occurrences in DED processes. That is, each build layer may be slightly thicker or thinner than the target layer thickness. Consequently, directly correlating position synchronized spectra and plume data captured during processing with a measured distance in the CT image introduces uncertainty along the z axis. Similar issues may also lead to uncertainty in the x and y locations. Uncertainty in the build-up direction is estimated to be on the order of the layer thickness (0.254 mm), while uncertainty in the x and y locations are expected to be much less than the hatch spacing (1 mm).

2.4.4 Graphical User Interface (GUI)

A graphical user interface (GUI) was designed as a tool for the manual analysis and comparison of each metric directly. The GUI was designed using object-oriented Matlab programming and a block digram representation of this code is shown in Appendix A.4

The program, as shown in Figure 2.8, allows a user to scroll through each deposition position and view each metric and its corresponding raw data at the same time. Using this information, a user can look for anomalies in the metrics and manually find the corresponding location within the CT image stack.

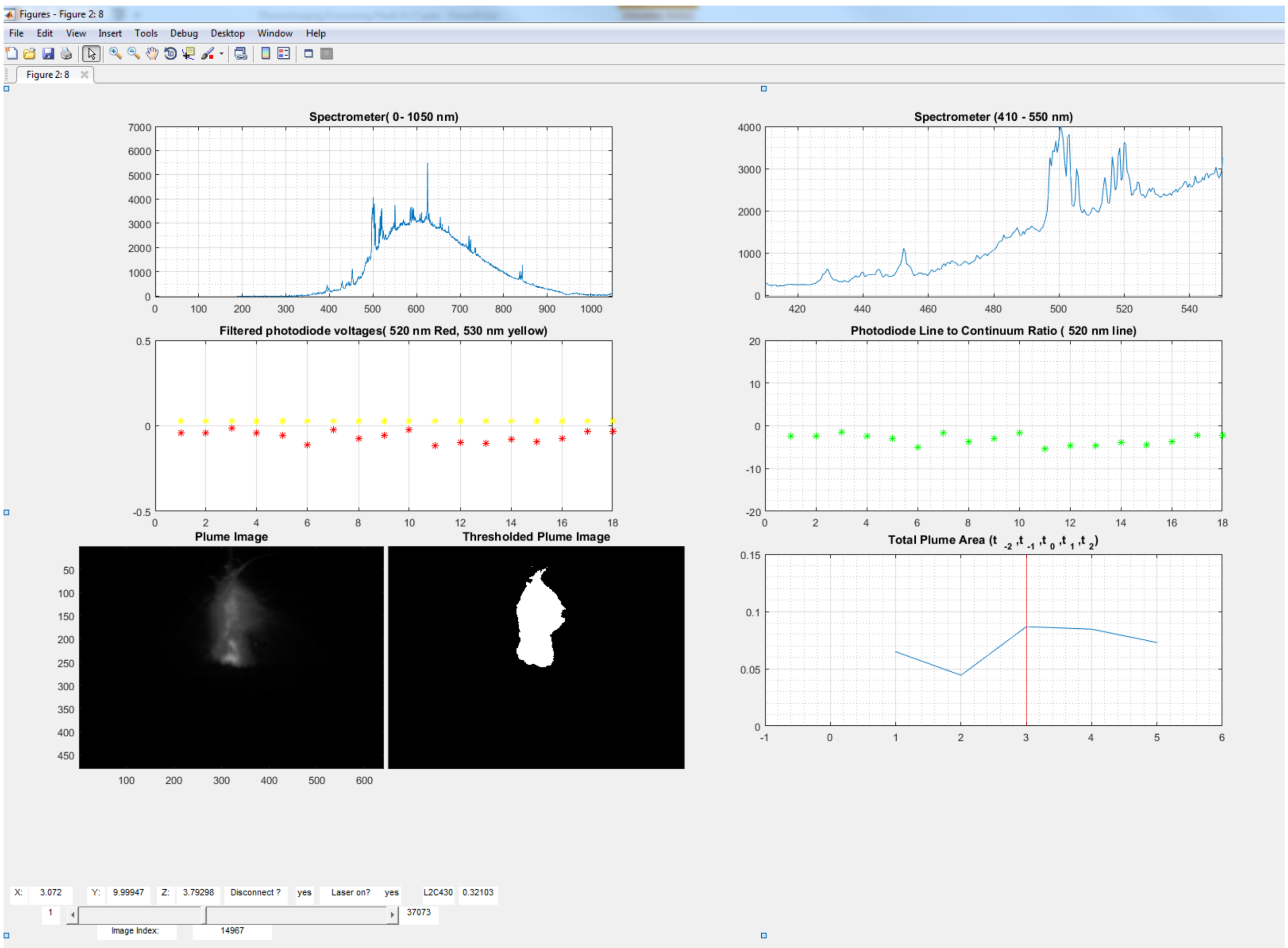

Figure 2.8: Graphical user interface showing each metric plotted at a particular time step.

Chapter 3

Results and Discussion

Results presented in Sections 3.1, 3.2, and 3.3 show that plume area and the line-to-continuum ratios around 430 and 520 nm are: 1) related to isolated, random discontinuities within an otherwise flaw-free build, 2) indicative of systematic flaws within a build, and 3) consistent with respect to one another. Here, an isolated, random flaw is defined as a discontinuity that appears in an otherwise dense component. This is in contrast to components containing systematic discontinuities, such as regular lack-of-fusion flaws resulting from non-ideal processing conditions.

3.1 Isolated Flaws

Plume area and the line-to-continuum ratios around 430 and 520 nm were affected by isolated, random flaws within an otherwise flaw-free component. To show this, two identically sized regions of interest (ROIs), one containing an isolated flaw and another without any flaws, were analyzed within the same component. During analysis, each ROI included at least three build layers, to account for over- and under-building. Figure 3.1 presents a representative image slice from each ROI, where Figure 3.1 (a) shows a region with an isolated discontinuity, and Figure 3.1 (b) shows a fully dense, flaw-free region. Both regions were from the same component (Run 11), and were thus processed under constant build conditions.

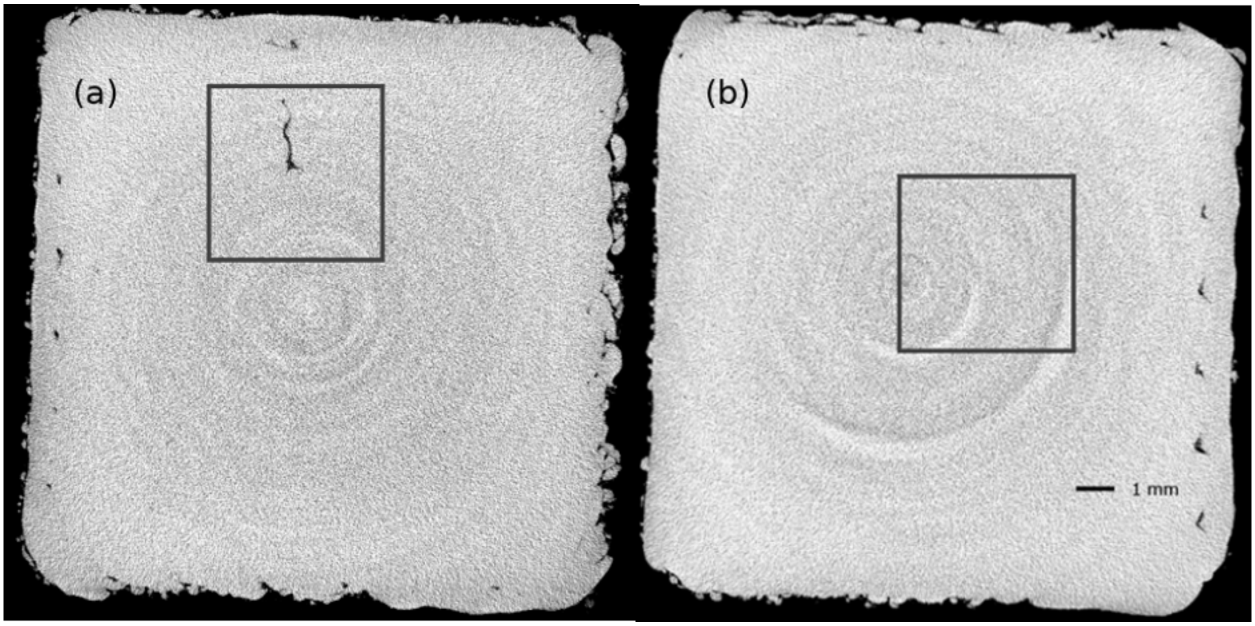

Figure 3.1: (a) CT slice with a discontinuity in the ROI. (b) CT slice from the flaw-free ROI.

Over the ROI containing an isolated discontinuity, shown in Figure 3.2 (a) and 3.2 (b), strong plume emissions were observed. The plume camera showed a significant increase in plume area which appears to have detached from the melt pool surface and propagates upwards, opposite to the beam propagation direction – this phenomenon is similar to that observed in optical discharges (e.g. laser-sustained plasma) [35]. Significant Ti I line emissions were also observed. Both line emissions and plume area fluctuated over this ROI. The largest plume area and most intense line emissions were estimated to occur in the region directly above the lack-of-fusion flaw that was observed in the CT scans. The physical relationship between the flaw and the observed plume fluctuations is not currently well understood, and is the subject of further investigation.

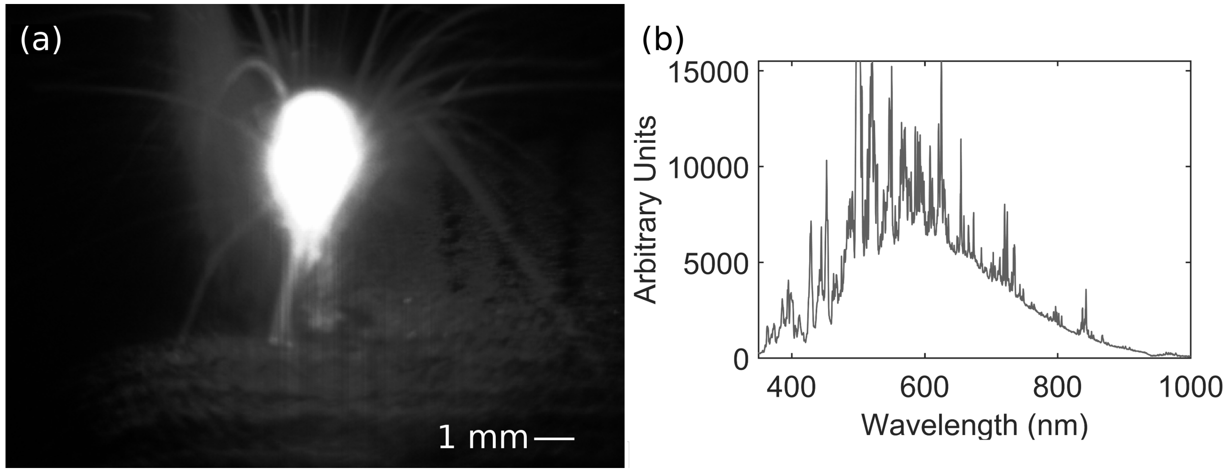

Figure 3.2: (a) Plume image from the ROI with the discontinuity. (b) Spectral signal from the ROI with the discontinuity.

Over the flaw-free ROI, shown in Figure 3.3(a) and 3.3(b), less intense plume emissions were observed. The plume camera observed a smaller plume that was located directly above the laser-material interaction zone. Ti I line emissions, that were prevalent in the isolated discontinuity region (Figure 3.2(b)), are not observed in the flaw-free region (Figure 3.3(b)). Instead, continuum spectra emissions are observed without obvious indication of line emissions and little fluctuation in intensity over time.

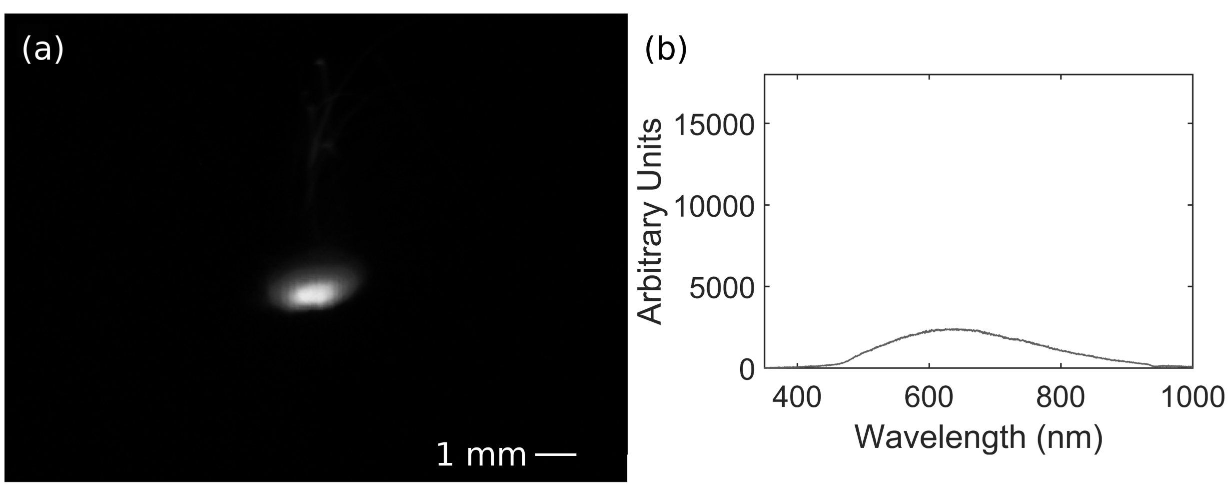

Figure 3.3: (a) Plume image from the flaw-free ROI. (b) Spectral signal from the flaw-free ROI.

3.2 Median Plume Metrics and Total Flaw Density

Plume metrics were also shown to relate to systematic discontinuities throughout a build, such as those resulting from non-ideal processing conditions. That is, for different runs under the same laser power but with varying powder flow rate and/or hatch pattern, the line-to-continuum ratios around 430 nm and 520 nm, and the total plume area increased as the flaw density of the build increased. As defined in Section 2.4.3, systematic discontinuities were measured using the flaw density (percentage of dense voxels to total voxels) within the interior of a build. A large flaw density is attributable to operating with sub-optimal processing parameters. Non-ideal processing conditions were observed to result in lack-of-fusion flaws, which are accounted for by calculating the flaw density. Figure 3.4 shows an example of the systematic flaws that occurred while using sub-optimal processing conditions in Run 008 (300 W, 4 g/min, parallel hatching). For each build, flaw density was compared to the median of each builds line-to-continuum ratio around 520 and 430 nm, as well as the median plume area.

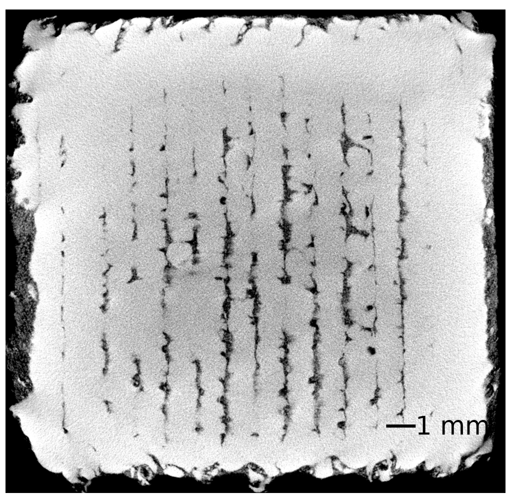

Figure 3.4: Systematic flaws found in Run 008 (300 W, 4 g/min, parallel hatching).

Figure 3.5 shows median line-to-continuum ratios and plume area plotted against the flaw density. It can be observed that, for a given laser power, an increase in the flaw density (caused by changes to powder flow rate and/or hatch pattern) is accompanied by an increase in each metric.

Furthermore, it is observed that an increase in laser power systematically shifts the metric values upward. This suggests that future work may lead toward the ability to predict changes in flaw density through observation of plume fluctuations caused by unexpected variations to other process parameters, e.g. an unanticipated reduction in powder flow rate, at a known laser power.

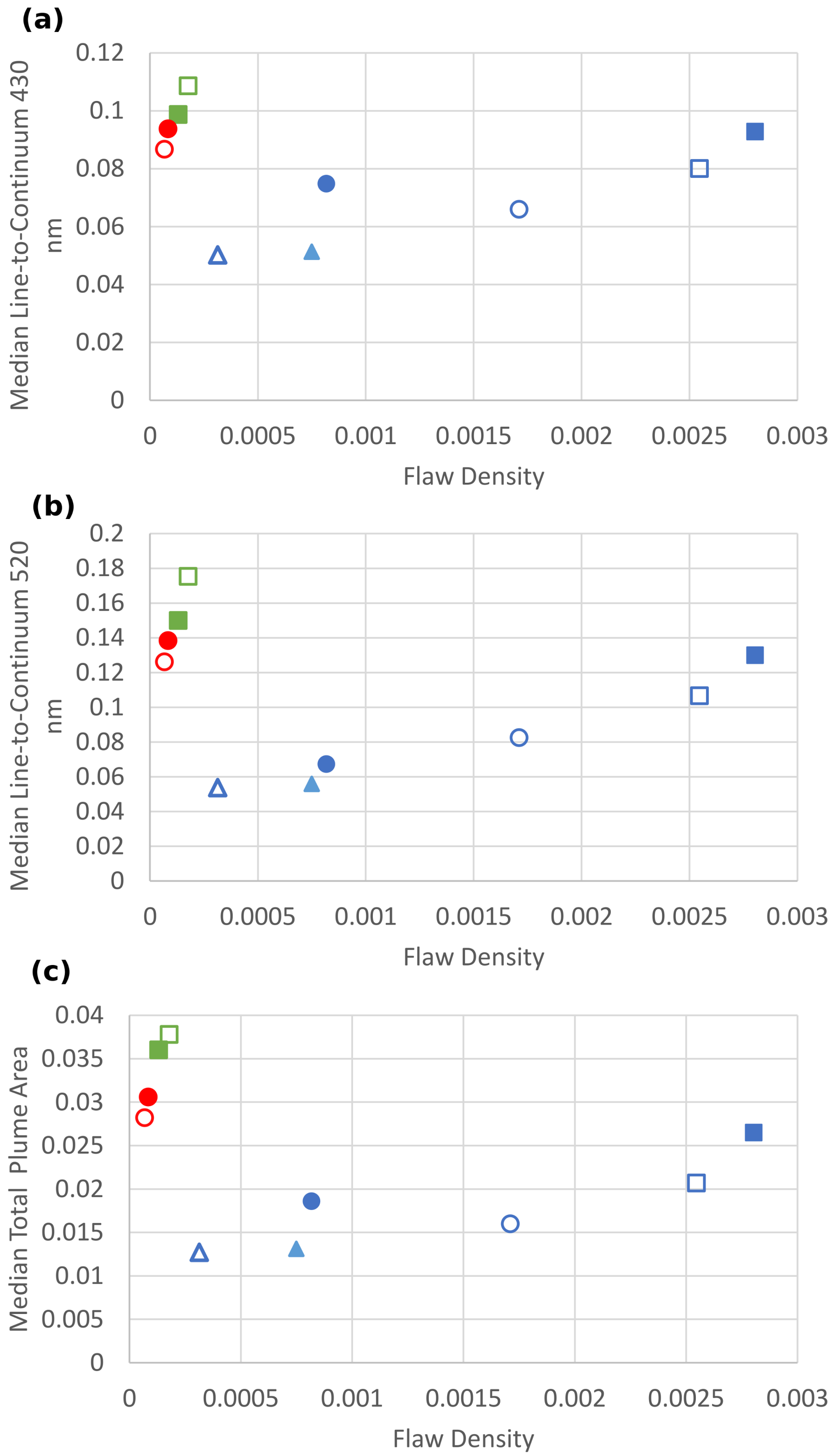

Figure 3.5: (a) Median L2C 430 plotted against flaw density. (b) Median L2C 520 plotted against flaw density. (c) Median total plume Area plotted against flaw density. Blue represents 300 W, Red represents 425 W, and Green represents 475 W. Triangles represent 2 g/min, circles represent 3 g/min, and squares represent 4 g/min. Filled shapes use a parallel hatch pattern, and open shapes use the cross hatch pattern.

3.3 Internal Consistency

Both the plume camera and the spectrometer were intended to measure the same phenomena, i.e. fluctuations in the state of the plume, during the build process. If this is true, then plume area and the line-to-continuum ratios should be internally consistent, i.e. they should show correlation to one another. To account for fluctuations in the collection rate of spectral emissions and plume images caused by lag in the system, spectral data were indexed to plume images by downsampling emissions spectra data. In cases where multiple spectra were collected during collection of one plume image, the spectra data were averaged.

Pearson correlation coefficient (r), a standard measure of the linear correlation between two variables, was calculated for each combination of plume metrics, e.g. (line-to-continuum ratio around 430 nm (L2C 430 nm) vs (total plume area), and are shown in Table 3.1.

Table 3.1: Pearson correlation coefficient (r) between each metric pair

Run #	Laser Power (W)	Powder Flow Rate (g/min)	Hatch Pattern	r-L2C 430 nm to total plume area	r-L2C 520 nm to total plume area	r-L2C 430 nm to L2C 520 nm
1	300	2	Parallel	0.0572	0.2368	0.3787
5	300	2	Cross	0.0359	0.3441	0.1905
6	300	3	Parallel	0.1914	0.444	0.5141
7	300	3	Cross	0.0799	0.4918	0.1835
8	300	4	Parallel	0.1755	0.5349	0.3721
9	300	4	Cross	0.1092	0.5762	0.2031
12	425	3	Parallel	0.5261	0.5994	0.8832
13	425	3	Cross	0.5545	0.6307	0.8739
20	475	4	Parallel	0.6213	0.6682	0.9275
22	475	4	Cross	0.6361	0.6741	0.938

For low laser power, a lower correlation coefficient was calculated, indicative of a weak linear correlation. However, with increasing laser power, the correlation coefficient between each pair of plume metrics increased significantly. Low correlation at low laser powers can be attributed to the low signal-to-noise ratio (SNR). At low laser powers, plume emissions are much less intense, yielding smaller line-to-continuum values and a small plume area. Here we are using measuring instruments that amplify the captured signal and any electromagnetic measurement noise equally. Since the sensing set-up remained undisturbed throughout all of the experiments, it can be assumed that the noise within the system should remain the same. Assuming the noise in the system is similar for all laser powers, builds with lower signal intensities will have a much smaller SNR. Nevertheless, even at low laser powers, there still exists some correlation between the plume metrics. For a higher laser power, a higher SNR resulted in higher correlation coefficients. At 475 W, a high linear correlation coefficient was observed between each pair of plume metrics i.e. the total plume area and L2C 430 as shown in Figure 3.6.

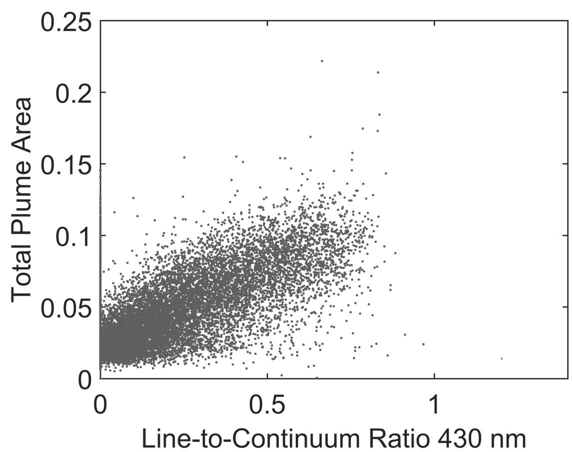

Figure 3.6: Linear relationship shown between two different metrics with a laser power of 475 W.

These results show that each sensor was indeed measuring the same phenomena—the plume—and that alternative sensor modalities which query the same phenomena may be realizable.

3.4 Issues Encountered

During data analysis, a few different issues were encountered that rendered some of the data collected to be unusable. While not a significant impedance to the overall effort, these issues provided useful information about problems with the methods considered.

3.4.1 Inconsistencies in Archimedes Density

An Archimedes density measurement was explored to quickly and inexpensively assess the flaw density of each coupon. Isopropyl alcohol was chosen to ensure proper wetting of the surface, and established procedures for the density measurement were followed, but measurement inconsistencies were found. First, the densities calculated using Archimedes method did not follow the same trend as those calculated using the CT method described in Section 2.4.3. Additionally, one outlier had a significantly higher density than all of the other parts. This outlier had a density significantly larger ($\sim$ 18%) than any published density value of Ti-6 Al-4V. Finally, all of the Archimedes densities that were calculated were very similar to each other. This leads to a debate on whether the results are actually statistically significant. The inconsistencies found can possibly be attributed to a few different sources. First, the balance used was last calibrated in 2014, and may have acquired some inaccuracies due to the long time period in between calibrations. Secondly, the test coupons had extremely rough surfaces. The surface roughness may contribute to the error by forming very small gas bubbles on the surface. These small gas bubbles can result in a lower than anticipated density. In addition, the laboratory in which the experiment was conducted was under construction when the data were collected. This caused large drafts to be present within the room, allowing large temperature and humidity fluctuations to occur. Considering all of these influences, the use of the Archimedes method was discontinued, and all analysis relied on the more expensive, and time consuming CT technique.

Chapter 4

Conclusions & Broader Impact

4.1 Conclusions

This work demonstrates that plume emissions are useful to assess build quality during DED AM operations. In particular, both isolated lack-of-fusion flaws in otherwise fully dense builds as well as builds with systematic discontinuities can be identified using the line-to-continuum ratio technique or the plume-imaging technique. Both measurement techniques are shown to interrogate the state of the plume. At this time, the specific physical phenomena which result in plume fluctuations are not well understood, and thus represent an important topic for additional investigation.

A limitation of the developed techniques is that low signal levels at low laser powers that yield low signal-to-noise ratio (SNR). With increasing laser power, plume emissions may be expected to rapidly increase before leveling off somewhat [35, 41, 45, 49]. Within the power ranges tested (300-475 W), this expectation was confirmed. The greatest utility of the developed technique is likely to be realized when processing at moderate to high laser powers (several hundred watts – kilowatts), depending on the materials interacting in the laser-processing zone.

The low data-acquisition rate used for this work is another limitation; it results in a limited temporal (and thus spatial) resolution for detection of anomalies. Both the spectrometer and plume camera operated with a capture rate of 50 Hz, i.e. data acquisition occur every 20 ms. During each captured period, the spectrometer integrated emissions for 20 ms and transmission of data did not impact the acquisition rate. However, the plume camera required 10 ms for data transmission, so exposure time was limited to 10 ms. In the experiments, the processing speed was 10.6 mm/s; so, the deposition proceeds 0.106 mm during the time it takes for a plume image to be returned. The consequence of this is that the plume camera may miss anomalies occurring over a length-scale smaller than 0.106 mm. Discontinuities occurring over a length-scale much smaller than 0.212 mm may also have a low SNR.

Through this work, significant progress toward the in-situ monitoring of flaws during additive manufacturing has been made. Large isolated discontinuities have been successfully correlated to shifts in plume metric values, a relationship between total coupon flaw density and median plume metric has been discovered, and the internal consistency of data produced from multiple sensors has been verified.

4.2 Future Work and Broader Impact

The results presented here offer many opportunities for future work in AM sensing. First, improved light-collection methods and alternative hardware systems — i.e. high-speed photodiodes, refined focusing optic set-ups, etc. — can be used to improve temporal/spatial resolution while maintaining high SNR. This improvement will allow for the detection of smaller flaws that could not be detected with the current setup. Toward this goal, the photodiode optics have been redesigned in order to prevent fiber damage, while still capturing spectral emissions at a high rate.

The techniques described here show promise for in-situ monitoring of flaws. Future work includes application of the plume size and line-to-continuum technique to other material systems that are commonly used in AM. In addition, the use of multiple sensing modalities affected by plume emissions, such as acoustic emissions and visible light, will help to make in-situ flaw detection a reality. Furthermore, the establishment of signal-processing strategies to enable robust flaw detection will enable the development of feedback-based control systems, thus moving the technology beyond simply monitoring the process to actively monitoring deposition quality. These techniques can determine if a build must either be stopped and scrapped to curtail losses, or must be re-processed to fix the flaw before processing continues. The successful implementation of in-situ flaw sensing and correction will likely lead to the proliferation of AM techniques in industries where a low quantity of flaws is required such as the aerospace and medical industries. In addition, the ability to fix the parts before subsequent layers are deposited, or interrupt the manufacturing process before additional value-adding steps are performed, can lead to lower part prices, and ecological benefits by reducing the amount of materials consumed and scrap produced. Finally, application of these techniques to other AM processes, such as powder-bed fusion, is a natural extension of this work and is currently being investigated.

Appendix A

Block Diagrams for Matlab Codes

This appendix presents, in lieu of providing the actual code, block diagrams of each Matlab function that was written .

A.1 Spectrometer Block Diagram

The following block diagram provides a high-level summary of the Matlab function that was written to process the spectrometer data that was collected. The main purpose of this function is to input the data, calculate the line-to-continuum ratio, and save the processed data as an object to be used in the data analysis step.

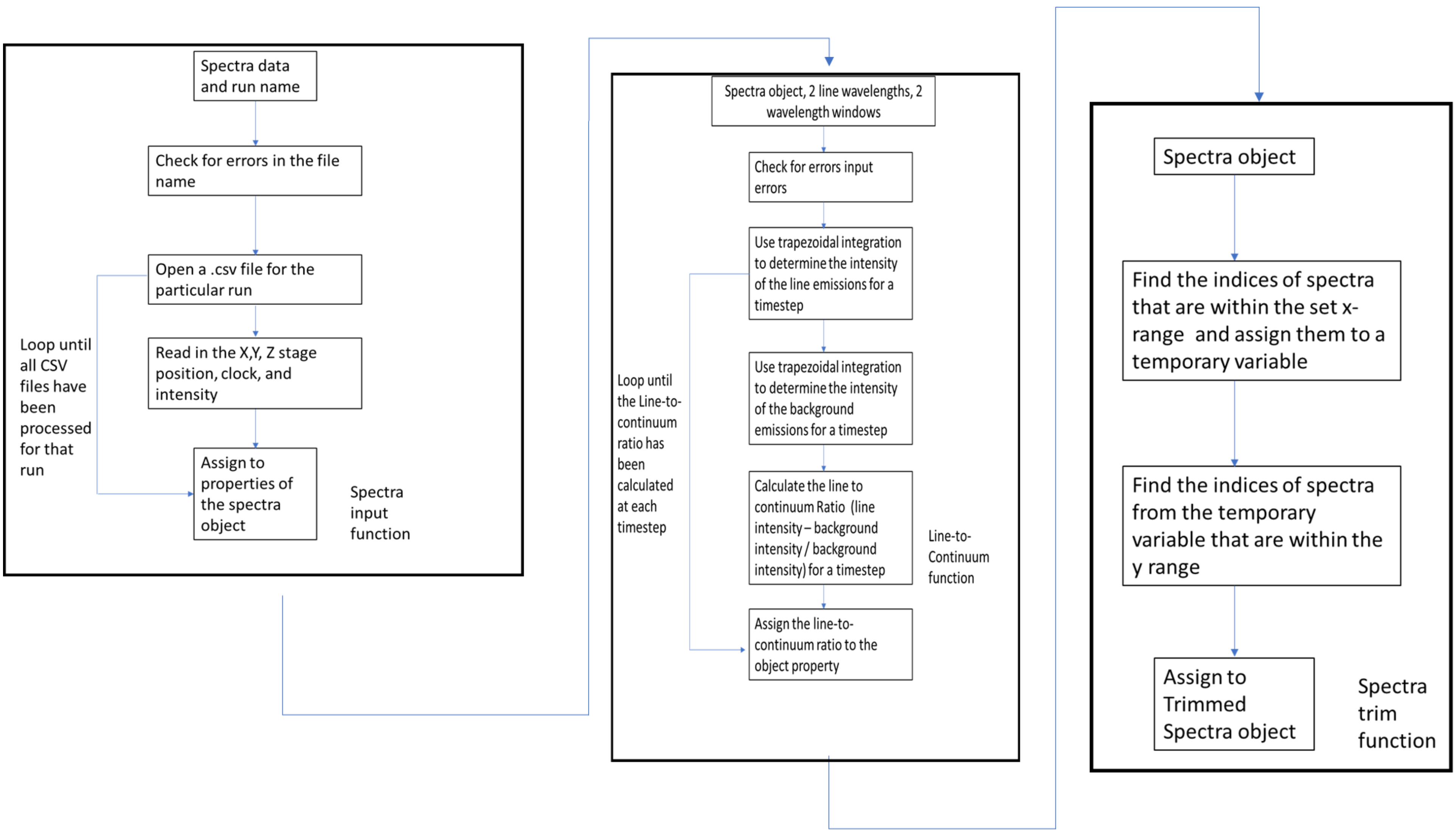
Spectra data and run name
Check for errors in the file name
Open a .csv file for the particular run
Read in the X,Y, Z stage position, clock, and intensity
Assign to properties of the spectra object
Loop until all CSV files have been processed for that run
Spectra input function
Spectra object, 2 line wavelengths, 2 wavelength windows
Check for errors input errors
Use trapezoidal integration to determine the intensity of the line emissions for a timestep
Use trapezoidal integration to determine the intensity of the background emissions for a timestep
Calculate the line to continuum Ratio (line intensity – background intensity / background intensity) for a timestep
Assign the line-to-continuum ratio to the object property
Loop until the Line-to-continuum ratio has been calculated at each timestep
Line-to-Continuum function
Spectra object
Find the indices of spectra that are within the set x-range and assign them to a temporary variable
Find the indices of spectra from the temporary variable that are within the y range
Assign to Trimmed Spectra object
Spectra trim function

A.2 Total Plume Area Block Diagram

The following block diagram provides a high-level summary of the Matlab function that was written to find the total plume area from each plume image. The main purpose of this function is to input each image, extract the position and time information, and calculate the total plume area, saving all data in an object to be used in the data analysis step.

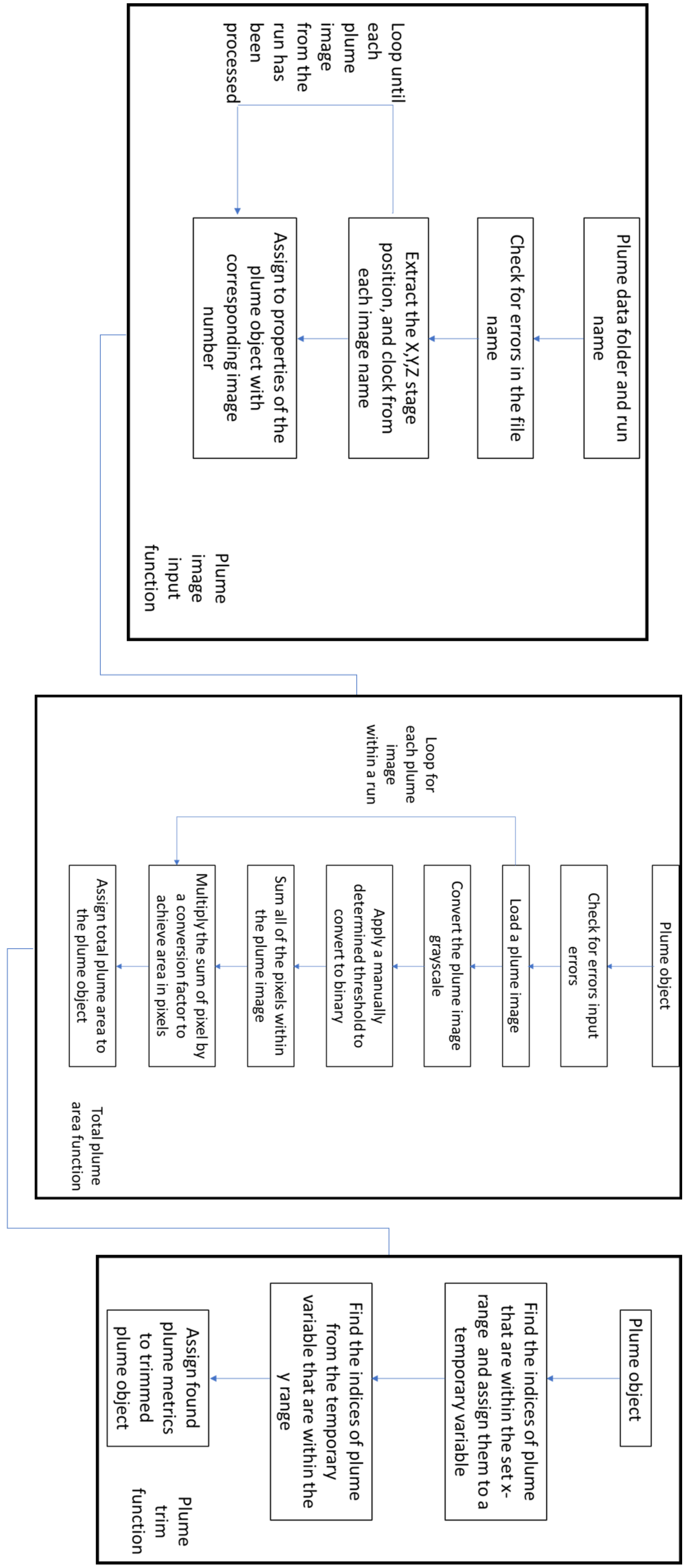
Plume image input function
Plume data folder and run name
Check for errors in the file name
Extract the X,Y,Z stage position, and clock from each image name
Assign to properties of the plume object with corresponding image number
Loop until each plume image from the run has been processed
Total plume area function
Plume object
Check for errors input errors
Load a plume image
Convert the plume image grayscale
Apply a manually determined threshold to convert to binary
Sum all of the pixels within the plume image
Multiply the sum of pixel by a conversion factor to achieve area in pixels
Assign total plume area to the plume object
Loop for each plume image within a run
Plume trim function
Plume object
Find the indices of plume that are within the set x-range and assign them to a temporary variable
Find the indices of plume from the temporary variable that are within the y range
Assign found plume metrics to trimmed plume object

A.3 CT Image Processing Block Diagram

The following block diagram provides a high-level summary of the Matlab function that was written to find the flaw density from each CT scan. The main purpose of this function is to input each tiff stack, calculate the number of void pixels on a layer, and calculate the total coupon flaw density, saving all data in a variable to be used in the data analysis step.

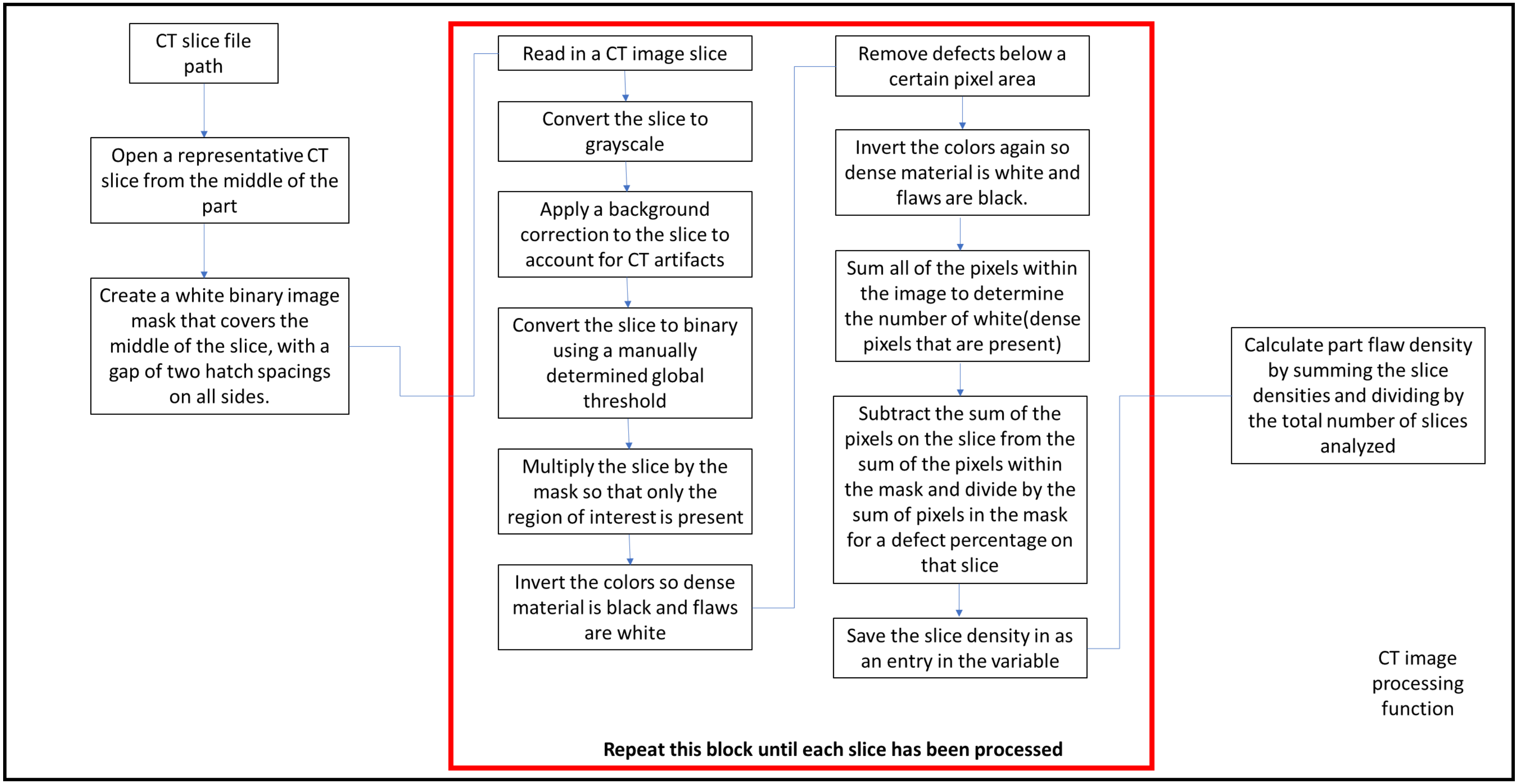
CT slice file path
Open a representative CT slice from the middle of the part
Create a white binary image mask that covers the middle of the slice, with a gap of two hatch spacings on all sides.
Read in a CT image slice
Convert the slice to grayscale
Apply a background correction to the slice to account for CT artifacts
Convert the slice to binary using a manually determined global threshold
Multiply the slice by the mask so that only the region of interest is present
Invert the colors so dense material is black and flaws are white
Remove defects below a certain pixel area
Invert the colors again so dense material is white and flaws are black.
Sum all of the pixels within the image to determine the number of white(dense pixels that are present)
Subtract the sum of the pixels on the slice from the sum of the pixels within the mask and divide by the sum of pixels in the mask for a defect percentage on that slice
Save the slice density in as an entry in the variable
Repeat this block until each slice has been processed
Calculate part flaw density by summing the slice densities and dividing by the total number of slices analyzed
CT image processing function

A.4 GUI Block Diagram

The following block diagram provides a high-level summary of the Matlab function that was written to analyze all of the data collected. The main purpose of this function is to take all of the data streams (line-to-continuum ratio, spectrometer capture, plume image, and total plume area) and plot them together for a specified time stamp. This function was designed such that a user can scroll through the time steps and compare each sensor and calculated metric to determine if any fluctuations occur.

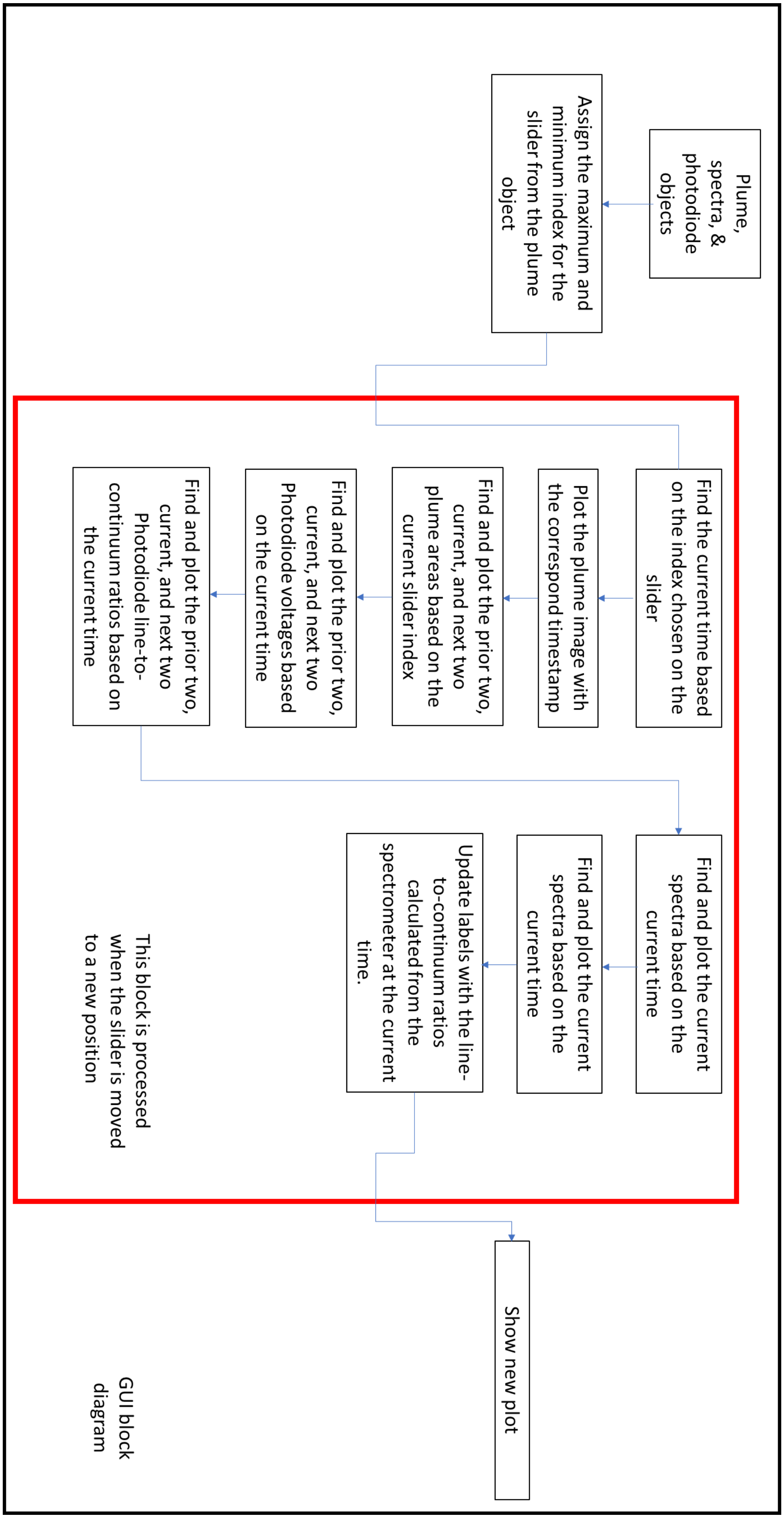
Plume, spectra, & photodiode objects
Assign the maximum and minimum index for the slider from the plume object
Find the current time based on the index chosen on the slider
Plot the plume image with the correspond timestamp
Find and plot the prior two, current, and next two plume areas based on the current slider index
Find and plot the prior two, current, and next two Photodiode voltages based on the current time
Find and plot the prior two, current, and next two Photodiode line-to-continuum ratios based on the current time
Find and plot the current spectra based on the current time
Find and plot the current spectra based on the current time
Update labels with the line-to-continuum ratios calculated from the spectrometer at the current time.
This block is processed when the slider is moved to a new position
Show new plot
GUI block diagram

Bibliography

[1] T. Kellner. How 3d printing will change manufacturing. Nov 2017. URL http://www.ge.com/reports/epiphany-disruption-ge-additive-chief-explains-3d-printing-will-upend-manufacturing.

[2] A. Bhargav, V. Sanjairaj, V. Rosa, L. W. Feng, and J. Fuh YH. Applications of additive manufacturing in dentistry: A review. *Journal of Biomedical Materials Research Part B: Applied Biomaterials*.

[3] D. Chen, S. Heyer, S. Ibbotson, K. Salonitis, J. G. Steingrmsson, and S. Thiede. Direct digital manufacturing: definition, evolution, and sustainability implications. *Journal of Cleaner Production*, 107:615–625, November 2015.

[4] R. Huang, M. Riddle, D. Graziano, J. Warren, S. Das, S. Nimbalkar, J. Cresko, and E. Masanet. Energy and emissions saving potential of additive manufacturing: thecase of lightweight aircraft components. *Journal of Cleaner Production*, 135:1559–1570, November 2016.

[5] W. E. Frazier. Metal Additive Manufacturing: A Review. *Journal of Materials Engineering and Performance*, 23(6):1917–1928, June 2014.

[6] R. Mudge and N. Wald. Laser Engineered Net Shaping Advances Additive Manufacturing and Repair. 86:44–48, 01 2007. URL http://www.rpm-innovations.com/uploads/lens_advances_manufacturing_and_repair.pdf.

[7] ANSI\AWS. Standard welding terms and definitions. ANSI A3.0-10, American National Standards Institute & American Welding Society, Washington, DC, 2010.

[8] ASTM. Standard terminology for additive manufacturing technologies. ASTM F2792-12a, American Society for Testing Material, West Conshohocken, PA, 2012.

[9] I. Gibson, D. W. Rosen, and B. Stucker. *Additive manufacturing technologies*. Springer US, Boston, MA, 2010.

[10] D. J. Corbin, A. R. Nassar, E. W. Reutzel, A. M. Beese, and N. A. Kistler. Effect of directed energy deposition processing parameters on laser deposited Inconel 718: External morphology. *Journal of Laser Applications*, 29(2):022001, May 2017.

[11] Z. Wang, T. A. Palmer, and A. M. Beese. Effect of processing parameters on microstructure and tensile properties of austenitic stainless steel 304l made by directed energy deposition additive manufacturing. *Acta Materialia*, 110:226–235, May 2016. ISSN 13596454.

[12] T. DebRoy, H.L. Wei, J.S. Zuback, T. Mukherjee, J.W. Elmer, J.O. Milewski, A.M. Beese, A. Wilson-Heid, A. De, and W. Zhang. Additive manufacturing of metallic components Process, structure and properties. *Progress in Materials Science*, 92:112–224, March 2018.

[13] D. Susan, J.D. Puskar, J.A. Brooks, and C.V. Robino. Quantitative characterization of porosity in stainless steel LENS powders and deposits. *Materials Characterization*, 57:36–43, July 2006.

[14] M. N. Ahsan, R. Bradley, and A. J. Pinkerton. Microcomputed tomography analysis of intralayer porosity generation in laser direct metal deposition and its causes. *Journal of Laser Applications*, 23(2):022009, May 2011.

[15] L. Wang, P. Pratt, S. D. Felicelli, H. El Kadiri, J. T. Berry, P. T. Wang, and M. F. Horstemeyer. Experimental analysis of porosity formation in laser-assisted powder deposition process. In *2009 TMS Annual Meeting & Exhibition*, February 2009. San Francisco, California.

[16] A. Sun, E. Kannatey-Asibu, and M. Gartner. Sensor systems for real-time monitoring of laser weld quality. *Journal of Laser Applications*, 11(4):153–168, August 1999.

[17] E. W. Reutzel and A. R. Nassar. A survey of sensing and control systems for machine and process monitoring of directed-energy, metal-based additive manufacturing. *Rapid Prototyping Journal*, 21(2):159–167, 2015.

[18] W. M. Steen and J. Mazumder. *Laser material processing*. Springer London, London, 2010.

[19] S. K. Everton, M. Hirsch, P. Stravroulakis, R. K. Leach, and A. T. Clare. Review of in-situ process monitoring and in-situ metrology for metal additive manufacturing. *Materials & Design*, 95:431–445, April 2016.

[20] G. Tapia and A. Elwany. A review on process monitoring and control in metal-based additive manufacturing. *Journal of Manufacturing Science and Engineering*, 136(6):060801–060801–10, October 2014.

[21] T. Purtonen, A. Kalliosaari, and A. Salminen. Monitoring and adaptive control of laser processes. *Physics Procedia*, 56:1218–1231, 2014.

[22] Mallikharjuna R. Boddu, Robert G. Landers, and Frank W. Liou. Control of laser cladding for rapid prototypingA review. In *Proceedings of the Solid Freeform Fabrication Symposium*, pages 6–8, August 2001. URL `http://citeseerx.ist.psu.edu/viewdoc/download?doi=10.1.1.462.8950&rep=rep1&type=pdf`. Austin, Texas.

[23] D. Hu and R. Kovacevic. Modelling and measuring the thermal behaviour of the molten pool in closed-loop controlled laser-based additive manufacturing. *Proceedings of the Institution of Mechanical Engineers, Part B: Journal of Engineering Manufacture*, 217(4):441–452, April 2003.

[24] D. A. Kriczky, J. Irwin, E. W. Reutzel, P. Michaleris, A. R. Nassar, and J. Craig. 3d spatial

reconstruction of thermal characteristics in directed energy deposition through optical thermal imaging. *Journal of Materials Processing Technology*, 221:172–186, July 2015.

[25] T. Craeghs, F. Bechmann, S. Berumen, and J.-P. Kruth. Feedback control of layerwise laser melting using optical sensors. *Physics Procedia*, 5:505–514, 2010.

[26] T. Furumoto, T. Ueda, M. R. Alkahari, and A. Hosokawa. Investigation of laser consolidation process for metal powder by two-color pyrometer and high-speed video camera. *CIRP Annals*, 62(1):223–226, 2013.

[27] D. Hu and R. Kovacevic. Sensing, modeling and control for laser-based additive manufacturing. *International Journal of Machine Tools and Manufacture*, 43(1):51–60, 2003.

[28] Z. Szymanski, J. Kurzyna, and W. Kalita. The spectroscopy of the plasma plume induced during laser welding of stainless steel and titanium. *Journal of Physics D: Applied Physics*, 30(22):3153, 1997.

[29] Hans R. Griem. *Plasma spectroscopy*. McGraw-Hill, New York, 1964.

[30] Hans R. Griem. *Spectral line broadening by plasmas*, volume 39. Academic Press, New York, 1974.

[31] A. Ancona, V. Spagnolo, P.M. Lugara, and M. Ferrara. Optical sensor for real-time monitoring of CO2 laser welding process. *Applied Optics*, 40(33):6019–6025, 2001.

[32] T. Sibillano, A. Ancona, V. Berardi, E. Schingaro, G. Basile, and P Mario Lugar. A study of the shielding gas influence on the laser beam welding of AA5083 aluminium alloys by in-process spectroscopic investigation. *Optics and Lasers in Engineering*, 44(10):1039–1051, October 2006.

[33] M. M. Collur and T. Debroy. Emission spectroscopy of plasma during laser welding of AISI 201 stainless steel. *Metallurgical and Materials Transactions B*, 20(2):277–286, April 1989.

[34] P. Sforza and D. de Blasiis. On-line optical monitoring system for arc welding. *NDT & E International*, 35(1):37–43, January 2002.

[35] A. R. Nassar, R. Akarapu, S. M. Copley, and J. A. Todd. Investigations of laser-sustained plasma and its role in laser nitriding of titanium. *Journal of Physics D: Applied Physics*, 45 (18):185401, May 2012.

[36] S. K. Tewari. *Plasma optical emission spectroscopy of laser cladding for process control and oxidation behavior of laser clad NbAl alloys*. PhD thesis, ProQuest Dissertations Publishing, 1995. Dissertation/Thesis.

[37] D. You, X. Gao, and S. Katayama. Data-driven based analyzing and modeling of MIMO laser welding process by integration of six advanced sensors. *The International Journal of Advanced Manufacturing Technology*, 82(5-8):1127–1139, February 2016.

[38] L. Song and J. Mazumder. Real time Cr measurement using optical emission spectroscopy during direct metal deposition process. *IEEE Sensors Journal*, (5):958–964, May 2012.

[39] L. Song, C. Wang, and J. Mazumder. Identification of phase transformation using optical emission spectroscopy for direct metal deposition process. In *Proceedings of SPIE*, volume 8239, February 2012. art no. 82390G.

[40] W. Ya, A. R. Konuk, R. Aarts, B. Pathiraj, and B. Huis in ‘t Veld. Spectroscopic monitoring of metallic bonding in laser metal deposition. *Journal of Materials Processing Technology*, 220:276–284, June 2015.

[41] K. Bartkowiak. Direct laser deposition process within spectrographic analysis in situ. *Physics Procedia*, 5(Part B):623–629, January 2010.

[42] L. Song, W. Huang, X. Han, and J. Mazumder. Real-time composition monitoring using support vector regression of laser-induced plasma for laser additive manufacturing. *IEEE Transactions on Industrial Electronics*, 64(1):633–642, January 2017.

[43] S. Liu, W. Liu, M. Harooni, J. Ma, and R. Kovacevic. Real-time monitoring of laser hot-wire cladding of Inconel 625. *Optics & Laser Technology*, 62(Supplement C):124–134, October 2014.

[44] A. R. Nassar, T. J. Spurgeon, and E. W. Reutzel. Sensing defects during directed-energy additive manufacturing of metal parts using optical emissions spectroscopy. In *Proceedings of Solid Freeform Fabrication Symposium (SFF)*. University of Texas Austin, TX, 2014.

[45] A. R. Nassar, B. Starr, and E. W. Reutzel. Process monitoring of directed-energy deposition of Inconel-718 via plume imaging. In *Proceedings of Solid Freeform Fabrication (SFF) Symposium, Austin, TX, USA*, 2015.

[46] C. B. Stutzman, A. R. Nassar, and E. W. Reutzel. Multi-sensor investigations of optical emissions and their relations to directed energy deposition processes and quality. *Additive Manufacturing*, (accepted).

[47] *LENS MR-7 Datasheet*. Optomec Inc, 2017. URL `https://www.optomec.com/wp-content/uploads/2014/04/LENS_MR-7_Datasheet_WEB_0816.pdf`.

[48] Curt Suplee. Atomic Spectra Database, July 2009. URL `https://www.nist.gov/pml/atomic-spectra-database`.

[49] J. Mazumder, T. J. Rockstroh, and H. Krier. Spectroscopic studies of plasma during cw laser gas heating in flowing argon. *Journal of Applied Physics*, 62(12):4712–4718, December 1987.

Academic Vita

Christopher B. Stutzman

EDUCATION

The Pennsylvania State University, *University Park, PA*

Bachelor of Science, Honors, Engineering Science — Graduation: May 2018
Student Marshal-- Department of Engineering Science and Mechanics
Schreyer Honors College
Engineering Mechanics Minor
Dean's List

Relevant Courses

Graduate Level Fundamentals of Additive Manufacturing, Wave Properties of Materials, Computational Methods using Matlab, Finite element analysis, Engineering Thermodynamics, Particulate Metal Processing, Phase Relations of Materials, Non-Destructive Analysis of Flaws, Advanced Engineering Mathematics, Thermal Properties of Material, Fluid Mechanics, Failure Analysis of Solid Materials

EXPERIENCE

Undergraduate Research Assistant, Center for Innovative Material Processing through Direct Digital Deposition (CIMP-3D), Penn State Applied Research Lab, University Park PA (January 2017- current)

- Implemented sensing equipment within additive manufacturing machines
- Collected and analyzed data to correlate process data to defects in an additively manufactured part
- Developed object-oriented Matlab scripts for data processing
- Presented research findings at an international additive manufacturing conference
- Authored, as primary author, a paper to be published in a peer-reviewed journal

Tutor, *Chemistry, Math, and Physics,* The Pennsylvania State University, Dunmore ,PA (August 2015 to May 2016) University Park, *Math* (August 2016 to January 2017)

- Helped students work through problems and understand where their learning deficit was
- Interacted with students of different cultures and learning styles

SKILLS

Microsoft Word, PowerPoint, Excel
Solidworks, Creo
Matlab, C++, Visual Basic
Labview
SEM
Public Speaking
Experimental Design
LaTeX

LEADERSHIP:

President, Penn State Worthington Music Club	Spring 2015 to May 2016
Lion Ambassadors	Fall 2014 to Summer 2016
Secretary, Penn State Society of Engineering Science	Fall 2017 to current
Penn State Worthington Science Mentor	Fall 2015

AWARDS:

Penn State Worthington Scranton Math award	2016
Penn State Worthington Scranton Honors Program	Fall 2014 to May 2016
Member, Tau Beta Pi	Fall 2016 to current

Presentations and Papers:

C. B. Stutzman, “Multi-sensor investigations of optical emissions and their relations to DED processes and quality,” presented at The Solid Freeform Fabrication Symposium (SFF), 09-Aug-2017, Austin Tx.

C. B. Stutzman, A. R. Nassar, and E. W. Reutzel, “Multi-sensor investigations of optical emissions and their relations to directed energy deposition processes and quality,” *Additive Manufacturing*.(accepted)